ChemComm

FEATURE ARTICLE

Cite this: *Chem. Commun.*, 2025, **61**, 8984

Received 8th April 2025,
Accepted 21st May 2025

DOI: 10.1039/d5cc01964h

rsc.li/chemcomm

Interface-assisted preparation of conductive MOF membrane/films

Yuxin Zhang,[a] Jing Zhang,[a] Fang Wang,[a] Gang Xu *[b] and Rui Zheng*[ac]

Conductive metal–organic frameworks (C-MOFs) are crucial electronic materials owing to their distinctive structures and intrinsic conductivities. C-MOF thin films enhance device integration, charge transfer, and the overall performance. The interface-assisted method has been proven to be effective for preparing high-quality thin films of C-MOFs. In this review, we outline various interface-assisted methods for preparing C-MOF thin films, including gas–liquid (G–L), liquid–liquid (L–L), and liquid–solid (L–S) interfaces, expound the growth mechanism of the interface-assisted method, introduce the applications of C-MOF thin films in electronic devices, and outline the development of the interface-assisted preparation of C-MOF membrane/films, pointing out potential challenges they may face.

1. Introduction

Metal–organic frameworks (MOFs) pertain to a class of crystalline porous substances featuring a periodic network architecture.[1–4] Compared to conventional materials, MOFs have gained favor among researchers due to their advantageous features, including adjustable ordered structure, substantial specific surface area, unoccupied metal sites, and high porosity.[5–13] Benefiting from their adjustable structure, large specific surface area, high porosity, and unsaturated active points, MOFs are widely used in gas adsorption and storage, bio-pharmaceutical health, catalysis, electrochemical energy storage, *etc.*[14–24] Conventional MOFs typically exhibit low electrical conductivity, a fundamental property that has restricted their broader adoption in advanced electronic systems requiring efficient charge transport.[22,25–27] MOFs usually contain a large number of organic ligands, which are mostly insulating. For example, common benzene dicarboxylic acid ligands (*e.g.*, terephthalic acid) are mainly composed of carbon,

---

[a] *School of Chemistry and Materials Science of Shanxi Normal University & Key Laboratory of Magnetic Molecules and Magnetic Information Materials of Ministry of Education, Research Institute of Materials Science of Shanxi Normal University, Taiyuan 030032, China. E-mail: yuxinzhang826@163.com, zhangjing@sxnu.edu.cn, wangfanghc@sxnu.edu.cn, zhengrui@sxnu.edu.cn*

[b] *State Key Laboratory of Structural Chemistry, Fujian Provincial Key Laboratory of Materials and Techniques toward Hydrogen Energy, Fujian Institute of Research on the Structure of Matter, Chinese Academy of Sciences, Fuzhou 350002, China. E-mail: gxu@fjirsm.ac.cn*

[c] *State Key Laboratory of Structural Chemistry, Fujian Institute of Research on the Structure of Matter, Chinese Academy of Sciences, Fuzhou 350002, P. R. China*

Yuxin Zhang

Yuxin Zhang is a master's student in the class of 2022, majoring in Chemistry at Shanxi Normal University. She is under the supervision of Prof. Fang Wang and Lecturer Rui Zheng. Her research interests include the preparation and properties of conductive MOF films and metal nanoparticles to further explore the potential applications of these materials.

Jing Zhang

Jing Zhang is working in the School of Chemistry and Materials Science, Shanxi Normal University, China. She received her PhD in 2022 from the Institute of Chemistry of the Chinese Academy of Sciences. Her main research focuses primarily on advanced two-dimensional semiconductor materials and functional devices, as well as bioelectrochemistry and electrocatalysis, which integrate various disciplines including chemistry, physics, materials science, and biology.

hydrogen, and oxygen in their molecular structures, and the covalent bonds formed by these elements are highly electrically insulating.[28] It is difficult for electrons to move freely in these ligands, thus limiting the electrical conductivity of the entire MOFs. In many MOFs, metal ions or metal clusters are tightly surrounded by organic ligands, and there is a lack of direct connecting channels between metal centres. Electrons cannot be transferred efficiently between the metal centres, resulting in poor conductivity.[29,30] The chemical bonding between metal ions and organic ligands in MOFs is mainly coordination bonding, which is intermediate in nature between covalent and ionic bonding. Unlike the strong conductivity of metallic bonds in metal crystals, coordination bonds have a lower degree of electron sharing and poor mobility of electrons, leading to poor conductivity.[31]

Conductive MOFs (C-MOFs) are a new family of MOF materials, which make up for the disadvantage of the non-conductivity of traditional MOFs and have great potential in the practical application of MOF material devices.[31–38] In addition to the advantages of traditional MOFs, C-MOFs also have unique physical and chemical properties, such as superior electrical conductivity, photoactivity, electrochemical activity, *etc.*, which endows C-MOFs in electronic devices and other fields with excellent application potential.[39–45] In addition to the advantages of traditional MOFs, C-MOFs also have unique physical and chemical properties, such as electrochemical activity, photoactivity, superior electrical conductivity, *etc.*, which endows C-MOFs in electronic devices and other fields with excellent application potential.[46] C-MOFs use organic ligands with large π-conjugation systems (*e.g.*, hexathiobenzene, tetrathiafulvalene TTF, porphyrin, *etc.*), where electrons can be delocalised in the conjugation system to form conductive channels,[47] and through π–π stacking form a tightly arranged layer or chain structure, which promotes electron hopping or off-domain conduction between neighbouring molecules. The electrical conductivity of some of the C-MOFs (*e.g.*, Cu-BHT, $\sim 10^3$ S cm^{-1}) are close to that of conducting polymers (*e.g.*, PEDOT:PSS, $\sim 10^4$ S cm^{-1}), but that of most of the C-MOFs is still lower than 1 S cm^{-1}. However, the C-MOFs have a long-range ordered crystalline structure, while the conducting polymers are mostly amorphous or partially crystalline.[48] Meanwhile, the pores of C-MOFs can be loaded with conducting guests (*e.g.*, TCNQ, I_2) to achieve dynamic modulation of conductivity. Enhanced electron delocalisation can be enhanced *via* ligand engineering *e.g.* by using ligands with large π-conjugation. It is also possible to introduce electron-donating/electron-absorbing groups (*e.g.*, $-NH_2$, $-NO_2$, $-CN$) for energy level modulation and enhanced charge transport. Conductivity can also be enhanced by metal node modulation, *e.g.*, selecting highly redox-active metals to promote electron hopping.[49]

The production of high-quality C-MOF thin films is crucial for the advancement of C-MOF devices.[50,51] Traditional film making techniques such as spin, spray, and drop coating often result in surface roughness and quality issues that do not meet the required standards. In addition, the deposition of particles creates numerous grain boundaries, significantly increasing the resistance to electron transmission. The main application

Fang Wang

Prof. Fang Wang serves as the Dean of the School of Chemistry and Materials Science, Shanxi Normal University, and the Deputy Director of the Key Laboratory of Magnetic Molecules and Magnetic Information Materials of the Ministry of Education. Her research focuses on advanced permanent magnets and magnetic two-dimensional materials. She has been honored as a Fellow of the Royal Society of Chemistry and recognized as a leading talent in scientific and technological innovation in Shanxi Province.

Gang Xu

Gang Xu received his PhD in 2008 at FJIRSM, CAS. Then he worked as a postdoctoral fellow at COSDAF in City University of Hong Kong (Hong Kong), University of Regensburg (Alexander von Humboldt fellowship, Germany) and Kyoto University (JSPS fellowship, Japan) in sequence. In 2013, he joined FJIRSM and undertook independent research as a PI. His research interests focus on the surface/interfacial coordination chemistry of materials and the related electrical devices.

Rui Zheng

Rui Zheng is a lecturer in the School of Chemistry and Materials Science, Shanxi Normal University, China. He graduated from the Fujian Institute of Structure of Matter, Chinese Academy of Sciences, with a PhD in Physical Chemistry in 2022, under the supervision of researcher Gang Xu. His main research interests include the growth mechanism of conductive MOF films and their electrical properties, preparation of metal nanoparticles and their properties.

Table 1 Comparison of interface-assisted methods with other methods

Method	Film quality	Crystalline	Preparation conditions
Interface-assisted method	Thin film	Good with orientation	Room temperature and pressure
Exfoliation and recombination	Mostly thick films	Poor	Easy
CVD	Mostly thick films	Good	High temperature

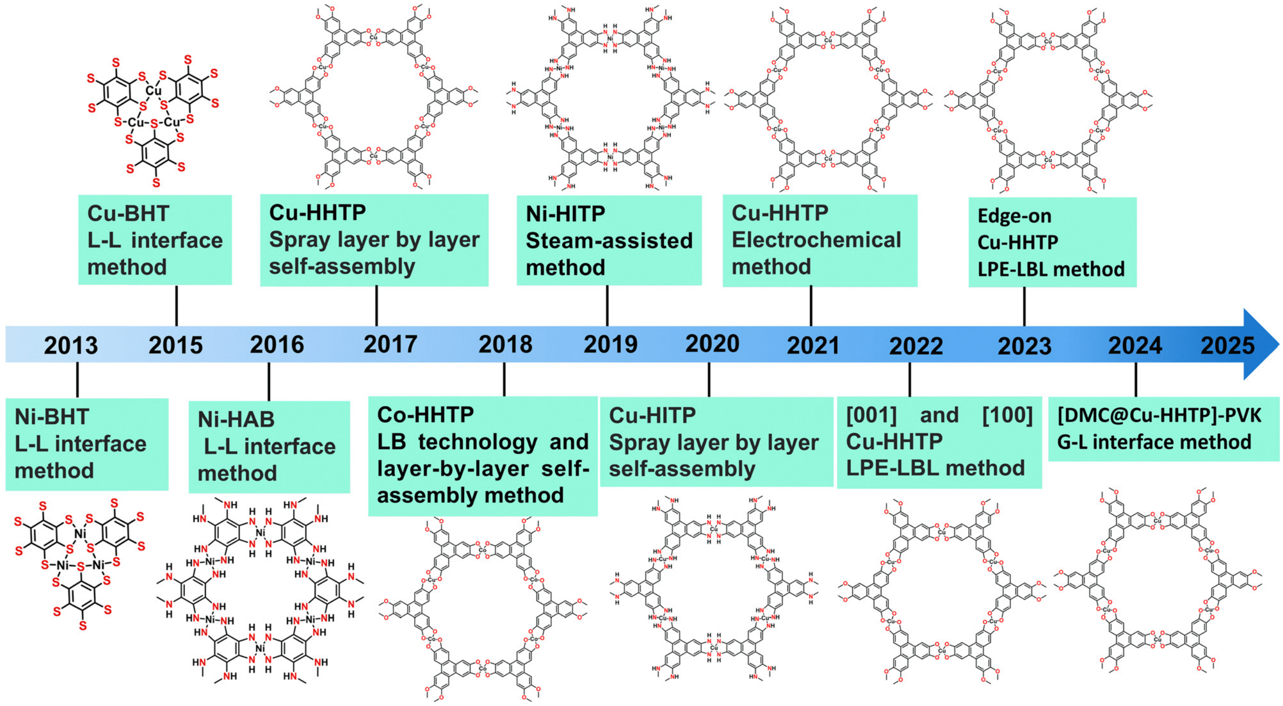

Fig. 1 Time axis of C-MOF membrane/films prepared using an interface-assisted method.

of C-MOFs in devices currently relies on powders or thick films, which hinder charge transfer and restrict the broader use of C-MOFs.[52] Extensive studies have been conducted on preparing high-quality C-MOF films to enhance the application potential in various devices.[53]

Three methods for preparing C-MOF films have been reported: exfoliation and recombination (ERA), chemical vapor deposition (CVD), and interface-assisted synthesis (Table 1).[54] The exfoliation and recombination method is straightforward and produces high yields, resulting in samples that effectively use active sites.[55,56] Nevertheless, this method exhibits inadequate shape control, a high density of defects, uneven grain size and thickness, and limited dimensions coupled with elevated defect rates, making it challenging for application in device fabrication. The viability of the CVD approach for synthesizing C-MOFs with high crystallinity has been demonstrated. Nevertheless, the problem of possible thermal deterioration of organic ligands and MOFs at elevated temperatures necessitates further solution.[57–59] The interface-assisted synthesis method exhibits a high degree of controllability throughout the synthesis process, with its interface serving as a template for the construction of C-MOF films, thereby facilitating the mitigation of ligand and inorganic salt diffusion limitations. The C-MOF films produced *via* this approach demonstrate several advantages, including high crystallinity, large size, controllable thickness, superior structural integrity, and remarkable mechanical stability.[56,60] As shown in Fig. 1, a time axis of the development of the interfacial-assisted synthesis method has been introduced from 2015 to the present.

Many reviews have been published on the preparation methods for C-MOF films. However, there is no specific review on the application of interfacial-assisted synthesis in the preparation of C-MOF films. This review details the principles and advantages of the interface-assisted synthesis of C-MOF thin films. The methods for interface-assisted synthesis are summarized, including G–L, L–L, and L–S interface-assisted synthesis. The growth mechanism of the interface-assisted synthesis is discussed. Applications of C-MOF thin-film devices, including FET, chemiresistive sensors, superconductors, and photodetectors, are introduced. Finally, insights into the challenges and future developments in the interface-assisted preparation of C-MOF membrane/films are provided.

2. MOF films prepared using an interface-assisted method

Interface-assisted synthesis represents a proficient methodology for the fabrication of large-area thin films in which a

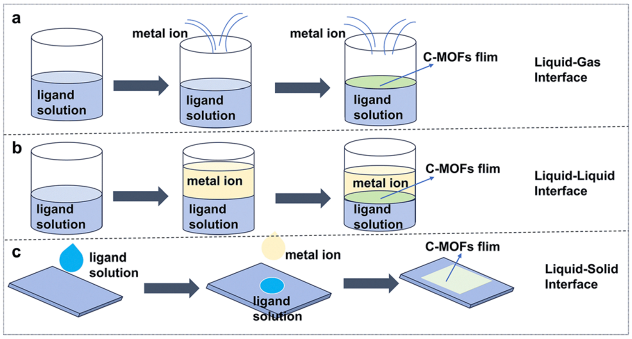

Fig. 2 Diagram of the interface-assisted method. (a) G–L interface; (b) L–L interface; and (c) L–S interface.

ligand is dispersed in one phase and the required inorganic salts are present in another incompatible phase. When these two phases come into contact, driven by the surface tension and intermolecular forces, a reaction occurs between them. During this process, the ligand gradually diffuses from the solution to the two-phase interface and reacts with the inorganic salt present in the other phase. As the reaction continues, the ligands in the two phases are gradually consumed, forming a film at the interface (Fig. 2).

The interface-assisted synthesis method primarily utilizes the G–L, L–L, and L–S interfaces to facilitate film deposition (Fig. 2).[61] In comparison to alternative methods, this approach offers several advantages: (1) it facilitates the preparation of large continuous films, utilizing its interface as a template for the construction of C-MOFs; (2) it is user-friendly, employing a straightforward methodology that allows for high control during the synthesis process; and (3) the proposed approach is cost-efficient while guaranteeing high efficacy. This methodology facilitates the *in situ* fabrication of C-MOF films through the direct connection of ligand molecules to metal atoms.

2.1. Liquid–liquid interface

In 2013, Hiroshi's group synthesized Ni-di(thiophene) nanosheets (Ni-BHT) consisting of two five-membered heterocycles and two sulphur atoms using the L–L interface method. The water phase contained nickel(II) acetate and sodium bromide, where sodium bromide was used as a source of charge-compensated counteracting ions (Na^+), and the organic phase (CH_2Cl_2) contained BHT.[62] The organic stratum was initially overlaid with deionized water, and subsequently, aqueous solutions of nickel(II) acetate and sodium bromide were carefully introduced into the deionized water stratum to preserve a tranquil L–L interface. After one day in argon, the substance transformed into a black solid featuring a metallic luster at the interface (Ni-BHT) (Fig. 3a). Ni-BHT was demonstrated to be a solitary chip with a transverse dimension of approximately 100 μm and a thickness ranging from 1 to 2 μm (Fig. 3b). In addition, selected area electron diffraction (SAED) showed a hexagonal diffraction pattern, indicating the formation of a hexagonal lattice (Fig. 3c). In 2015, the team also used a L–L interface reaction to prepare Pd-BHT, dissolved K_2PdCl_4 and NaBr in water, and reacted BHT at the L–L interface in organic dichloromethane.[63] The Na ions in the added sodium bromide (NaBr) act as counter-anions to balance the charge of the palladium-di-*tert*-butyl p-cresol (Pd-BHT) anion (*i.e.*, [bis(disulfide) palladium(III)]). After the two-phase solution was left overnight, a black film formed at the interface (Fig. 3d). The thickness of the Pd-HTB film was approximately 2–3 microns. In order to inhibit the formation of palladium nanoparticles (Pd NPs), potassium ferricyanide ($K_3[Fe(CN)_6]$) was introduced into the aqueous layer prior to the commencement of the L–L interface reaction. This was because $K_3[Fe(CN)_6]$ functioned as a redox buffer, thereby preventing the reduction of Pd^{2+} ions. Scanning probe microscopy (SPM) measurements showed that nano-Pd-HTB had a hexagonal ordered monolayer structure (Fig. 3e).

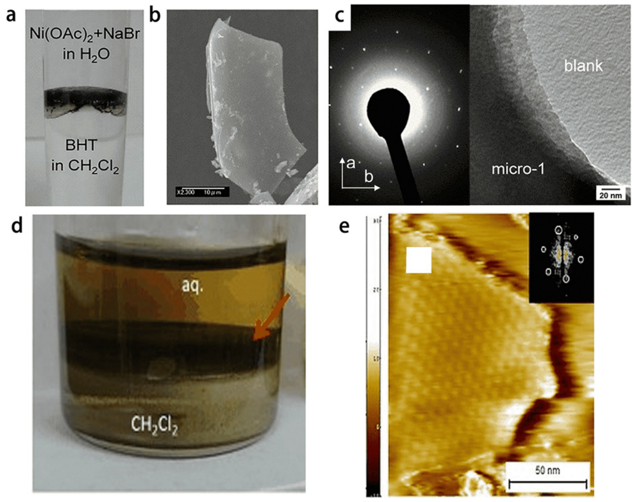

Fig. 3 (a) Photograph of Ni-HTB film synthesis at the water–DCM interface. (b) Scanning electron microscopy (SEM) image of the Ni-HTB film. (c) TEM image and SAED pattern of the Ni-HTB film. (d) Optical photograph of micro-PdBHT. (e) SPM images of nano-PdHTB. (Adapted from ref. 55 and 56 with permission from American Chemical Society, and John Wiley and Sons, Copyright 2013 and 2015, respectively.)

Zhu and colleagues prepared a high-quality C-MOF thin film (Cu-HTB) through a L–L interface reaction between copper(II) nitrate/water (aqueous phase) and BHT/dichloromethane (organic phase).[64] Two transfer methods were used to obtain the upper and lower films on the surface in contact with water, respectively. The optical image shows that the upper surface of the film was smooth and had a metallic luster, while the lower surface was rough and appeared matte black (Fig. 4a). The SEM images provide a more detailed display of the morphological differences on both sides of the membrane. The upper part is flat, has low roughness, and is continuous on a large scale without steps or cracks (Fig. 4b). The other side was rougher because of the randomly oriented sheet-like nanosheets (Fig. 4c). Four-probe measurements demonstrated that an electrical conductivity of the material at ambient temperature of 1580 S cm^{-1} could be attained. The material manifested bipolar charge transport characteristics and exhibited exceedingly high electron and hole mobilities under field-effect modulation (with electron mobility being 116 $cm^2\ V^{-1}\ s^{-1}$ and hole mobility being 99 $cm^2\ V^{-1}\ s^{-1}$).

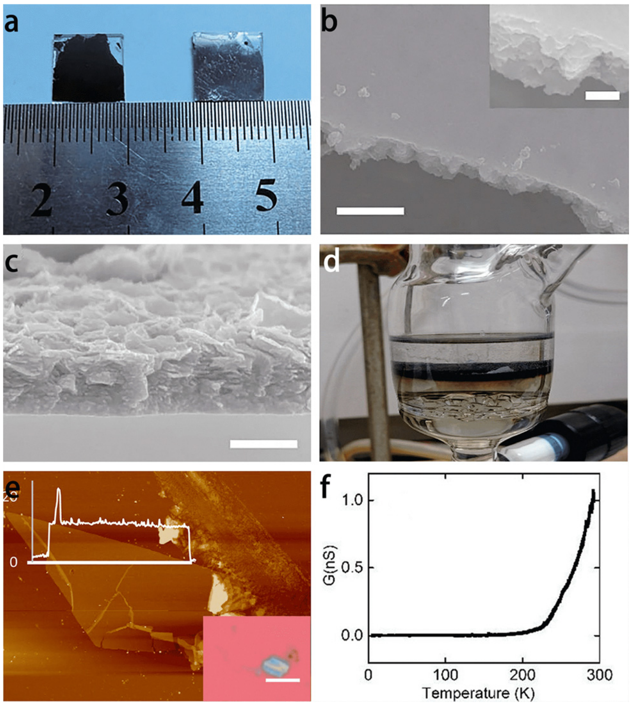

Fig. 4 (a) Photographs of the upside-up (right) and upside-down (left) films transferred onto glass substrates. (b) and (c) SEM image of the upside and cross-section of a 200-nm-thick film; the inset in (b) shows the details of the film edge with an enlarged scale. Scale bar: 200 nm in (b), 400 nm in (c), and 100 nm in the inset. (d) Optical photos of the M-HAB synthesis process. (e) AFM images of Ni-HAB. (f) Temperature-dependent conductance of Ni-HAB. (Adapted from ref. 57 and 58 with permission from Springer Nature, and American Chemical Society, Copyright 2015 and 2017, respectively).

In 2017, Janis and colleagues utilized the L–L interface to synthesize M-HAB (M = Ni, Cu, and Co) (Fig. 4d).[65] HBA has a bromine atom at each end, connected by a hexamethylene chain. First, after degassing, hexamethylene bromide (HAB) was dissolved in deionized water to form a homogeneous aqueous phase solution. Subsequently, M(acac)$_2$ (M stands for Ni, Cu, or Co, and acac for ethyl acetoacetate) solution was carefully added dropwise onto the surface of the aqueous phase. Under static solution conditions, as ethyl acetoacetate underwent gradual evaporation, a thin film spontaneously formed at the interface between the organic and aqueous phases. Atomic force microscopy (AFM) images showed that the resulting film had a uniform crystalline surface without any significant cracks (Fig. 4e). Subsequently, the electrical conductivity of the devices fabricated from various nickel nanosheets was evaluated at different temperatures, and it was observed that the electrical conductivity diminished with decreasing temperature, indicating insulating behavior during charge transfer (Fig. 4f).

In 2018, Qi's group reported a simple spray-assisted MOF synthesis strategy for rapidly and controllably preparing large-area MOF films at room temperature.[66] A nebulized Cu^{2+}-containing solution (DMF/CH$_3$CN, $V_{\mathrm{DMF}}:V_{\mathrm{CH_3CN}} = 1:2$) was precisely deposited onto the surface of a DMF/CH$_3$CN ligand solution ($V_{\mathrm{DMF}}:V_{\mathrm{CH_3CN}} = 2:1$, containing 1,4-benzenedicarboxylate) at a controlled flow rate of 1 μL s^{-1}. Within 30 seconds of deposition, a blue crystalline film emerged at the L–L interface, indicative of C-MOF nucleation and growth. Following the deposition of 50 mL precursor solution, a freestanding blue C-MOF membrane spontaneously assembled at the liquid–liquid interface. SEM analysis revealed a hierarchical architecture consisting of horizontally aligned square nanoplates (∼200 nm edge length) organized into lamellar superstructures with a periodic spacing of ∼610 nm (Fig. 5a and b). The film thickness exhibited precise tunability across the range of 0.25–5.55 mm through controlled modulation of the injected metal ion precursor volume. Notably, the system demonstrated exceptional copper ion utilization efficiency, achieving a remarkable 90% conversion rate of Cu^{2+} into the crystalline framework. Su *et al.* synthesized the thiol organic ligand phenylhexyl mercaptan (BHT) using a simple one-pot reaction using hexafluorobenzene and sodium isopropyl sulfate as raw materials.[67] This straightforward approach is not only safer but also quicker compared to conventional synthesis techniques, which necessitate the use of liquid ammonia as a solvent. Subsequently, two novel C-MOF materials, Ag-HTB and Au-HTB, were prepared by

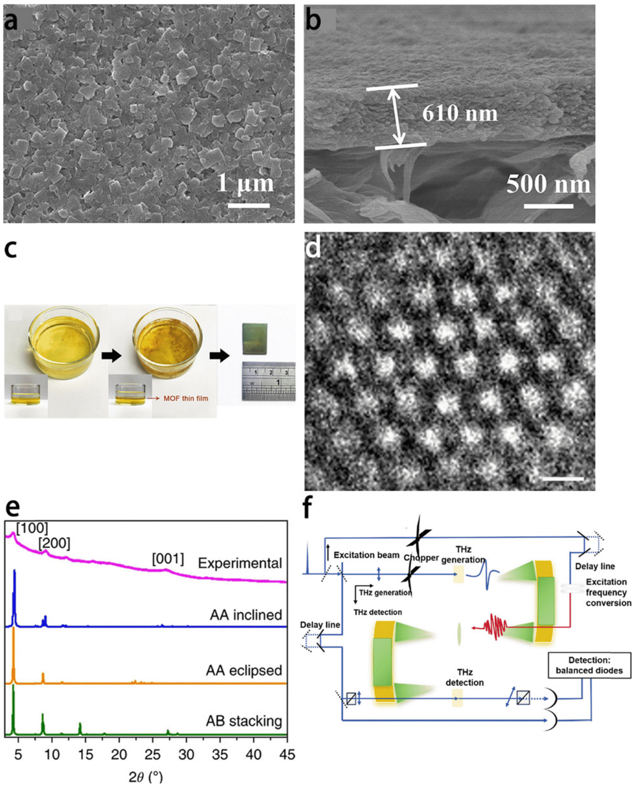

Fig. 5 (a) SEM top-view image and (b) cross-sectional SEM image of Cu-BDC thin film. (c) Optical photograph of the Ag/Au-BHT film prepared using the L–L synthesis method. (d) HR-TEM image of the 2D honeycomb structures. Scale bar, 2 nm. (e) Experimental and calculated PXRD patterns of the DFT-optimized structures. (f) Schematic representation of the optical pump-THz probe experimental setup. (Adapted from ref. 59–61 with permission from American Chemical Society, and American Chemical Society, Copyright 2018 and 2018, respectively.)

coordinating Ag or Au ions with BHT through an L–L interface reaction (Fig. 5c).

Feng and his team utilized the L–L interface approach to fabricate a C-MOF $Fe_3(THT)_2(NH_4)_3$ thin film. In this process, the aqueous phase was composed of THT, while the $CHCl_3$ phase contained iron precursors.[68] Under room temperature argon gas conditions, spontaneous $CHCl_3$/water interface reactions could form large independent multilayer films without steps or cracks. High-resolution transmission electron microscopy (HR-TEM) revealed a honeycomb-like structure featuring a pore dimension of roughly 1.9 nm (Fig. 5d), and powder X-ray diffraction (PXRD) at 2θ peaks of (100) and (200) were observed at 4.5°and 9.1° (Fig. 5e), respectively, indicating hexagonal stacking in the *ab* plane. (001), peaking at 27.3°, shows ordered *c*-direction stacking with an interlayer distance of about 0.33 nm. The team conducted TRTS experiments on the $Fe_3(THT)_2(NH_4)_3$ C-MOF thin film to understand its charge transport properties (Fig. 5f).[69] Femtosecond laser pulses injected charges into the material, and measured changes in conductivity using ~1 ps terahertz pulses on an ultrafast time scale.

M-HHTP (where M(II) represents Co, Ni, and Cu) was initially described by Yaghi and his team as a bulk solid obtained through solvothermal synthesis. HHTP consists of three benzene rings arranged in a 'spoke-like' co-planar arrangement with a hydroxyl group attached to each of its six positions. In 2018, Tatay *et al.* carefully injected HHTP-dissolved ethyl acetate into an aqueous copper(II) acetate solution.[70] Following a few minutes, a pale blue Cu-HHTP film began to form at the interface between the water and the organic solvent. As the reaction progressed, the thickness of this film grew accordingly (Fig. 6a). The AFM analysis revealed that the thickness of the Cu-HHTP films prepared using this technique ranged from 10 to 70 nm (Fig. 6b). This approach has recently been employed to create thicker films composed of 2D π-conjugated MOFs, with thicknesses ranging from 100 to 350 nm (Fig. 6c and d).[63,64,71] The results indicate that this method is unsuitable for producing homogeneous Cu–HHTP ultrathin films smaller than 50 nm.

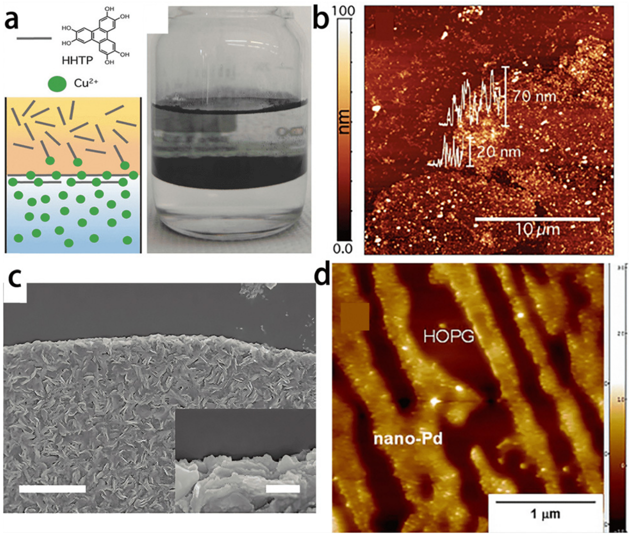

Fig. 6 (a) Schematic of the L–L interfacial method for fabricating Cu-HHTP thin films and a photograph of the Cu-HHTP film formed at the interface between the organic and aqueous solutions. (b) AFM topographic image of the Cu-HHTP film transferred to Si/SiO_2 substrates. (c) SEM images of the Cu-BHT film. Scale bar: 400 nm, and 100 nm in the inset. (d) AFM images of the Pd-BHT film. (Adapted from ref. 63, 57 and 56 with permission from John Wiley and Sons, Springer Nature, and John Wiley and Sons, Copyright 2018, 2015 and 2015, respectively).

2.2. Gas–liquid interface

In 2015, Feng *et al.* disclosed the preparation of large-scale, standalone monolayer Ni-THT membranes through Langmuir–Blodgett (LB) assisted interface synthesis and by regulating the surface pressure.[72] In the LB tank, a blend of the ligands HTTP and DMF/chloroform (volume-to-volume ratio = 1 : 3) is dispersed on the water surface (Fig. 7a). Following this, the surface pressure was measured and gradually raised to 10 mN m^{-1}, which packed the HTTP molecules tightly into a densely organized self-assembled monolayer. An aqueous solution containing nickel(II) nitrate was added to the water phase. As the Ni^{2+} ions diffuse towards the gas/water interface, a coordination reaction occurs between HTTP and Ni^{2+} ions to obtain a standalone single-layer Ni-THT film (Fig. 7b and c).

Xu's team used an innovative G–L interfacial method to prepare ultra-smooth and dense Ni-HITP films.[71] During their experiments, they first mixed an aqueous solution of HATP-6HCl (with HATP representing 2,3,6,7,10,11-hexamethylaminotriphenylene), $NiCl_2$–$6H_2O$, and trimethylamine, and heated the mixed solution to 60 °C. At this temperature, Ni^{2+} ions react at the G–L interface with the hexamethylaminotriphenyl ligand (HITP) generated *in situ* in a coordination reaction to form Ni-HITP nanoparticles by self-assembly. These generated Ni-HITP nanoparticles are hydrophobic; therefore, they naturally float on the water surface. These floating nanoparticles formed a 'smooth substrate' structure on the water surface (Fig. 7d). Due to the confinement effect at the G–L interface, the nanoparticles were able to pack tightly together, resulting in a uniform film layer with a thickness of only nanometers (Fig. 7e). After precise measurement, the size of this film is 20 μm × 20 μm, while the average roughness in this region is only 1.43 nm (Fig. 7f). This ultra-smooth and dense Ni-HITP film exhibited excellent properties in terms of both microstructure and surface properties, providing an important material basis for applications in related fields.

Rie *et al.* assembled uniaxially oriented C-MOF nanosheets synthesized from HITP and Ni^{2+} at the gas/liquid interface and confirmed the orientation and structure of the nanosheets using synchrotron X-ray (Fig. 8a and b).[73] The nanosheets exhibited a multilayer configuration, with a thickness of 14 nm, as well as high crystallinity and uniaxial alignment (Fig. 8c inset). First, the Langmuir tank was filled with a $Ni(OAc)_2{\cdot}4H_2O$ aqueous solution in polytetrafluoroethylene (PTFE), and then a microinjector was used to diffuse the solution of HATP onto the nickel acetate aqueous phase at room temperature. The nanosheets were then transferred to the substrate and their conductivities were measured. Based on the

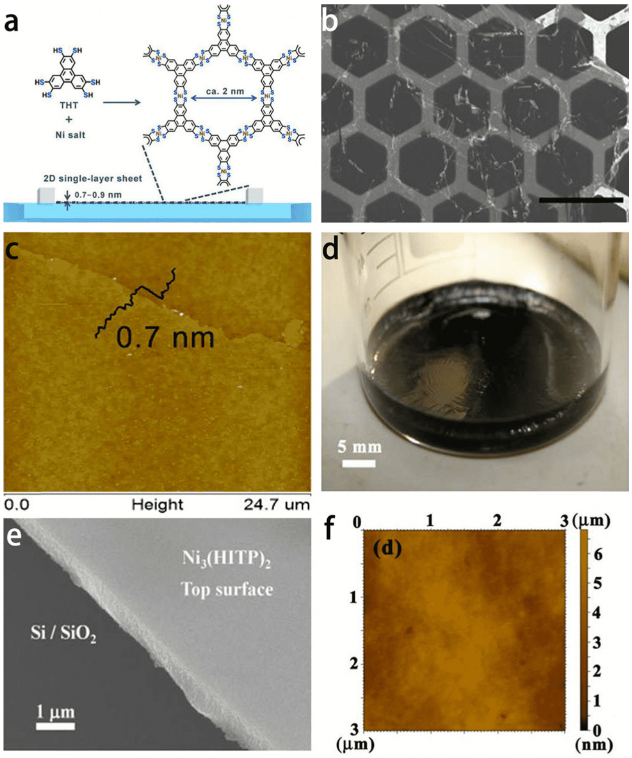

Fig. 7 (a) Single-layer 2D C-MOF films fabricated through LB-aided interfacial synthesis. (b) and (c) SEM and AFM images of single-layer Ni-THT (holes in a hexagonal shape having a side length of 18 μm). (d) Photograph of a $Ni_3(HITP)_2$ membrane forming at the gas–liquid interface. (e) SEM and (f) AFM images of the top surface of the $Ni_3(HITP)_2$ membrane. (Adapted from ref. 65 and 64 with permission from John Wiley and Sons, and American Chemical Society, Copyright 2015 and 2017, respectively.)

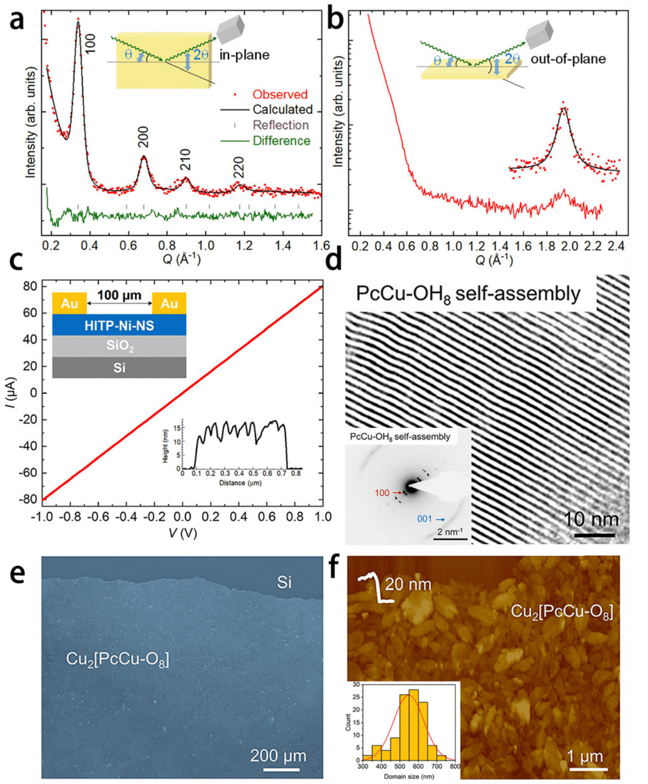

Fig. 8 (a) and (b) Structural characterization of HITP-Ni-NS by synchrotron XRD measurements. (c) Current(I)–voltage(V) curve for a device; inset: corresponding height profile of the film. (d) HR-TEM image of the self-assembly of PcCu–OH_8; inset: SAED pattern of the self-assembly of PcCu–OH_8. (e) SEM image of $Cu_2[PcCu–O_8]$ film. (f) AFM image of the $Cu_2[PcCu–O_8]$ film, inset: size distribution of $Cu_2[PcCu–O_8]$ crystals. (Adapted from ref. 67 and 68 with permission from American Chemical Society, and American Chemical Society, Copyright 2021 and 2021.)

I–V curve, the conductivity of the HHTP Ni-NS-5c sample, which consists of five layers, was determined to be 0.6 S cm^{-1} (Fig. 8c).

Feng's group utilized (2,3,9,10,16,17,23,24-octahydroxyphthalocyanine) metal (PcCu–OH_8 or PcFe–OH_8) as a ligand and square planar metal bis(dihydroxy) complexes as links for the synthesis of unprecedented $Cu_2[PcM–O_8]$ (M = Fe or Cu) C-MOF thin films facing the edge layer at the air/water interface.[74] Owing to the π–π interaction and the hydrophobic nature of the phthalocyanine ligand, its basal plane is oriented perpendicularly to the water surface. TEM and SAED patterns indicate that the PCC–OH_8 ligand is preorganized into an ordered two-dimensional network stacked edge-to-edge on the water surface before coordination assembly (Fig. 8d). SEM and light microscopy (OM) images showed macroscopically uniform films with dimensions exceeding square centimeters (Fig. 8e). AFM showed that the resulting film consisted of flat crystalline nanosheets with a thickness of about 20 nm and a lateral dimension on the order of several hundred nanometers (Fig. 8f).

Feng and his colleagues have recently devised a novel organic-liquid-gallium surface synthesis (OLGSS) approach under CVD conditions to achieve the controlled formation of C-MOF films (Fig. 9a).[75] The core of this strategy is based on a layer-by-layer (LBL) CVD growth model, which achieves uniform film growth by precisely controlling the chemical reactions and deposition conditions during the growth process. Liquid gallium (Ga) plays a key role in this process. The strong adhesion energy between aromatic ligands and liquid gallium not only promotes strong bonding of the ligands on the gallium surface but also triggers the LBL growth mode, which enables the 2D C-MOF films to grow uniformly and in an orderly manner on the gallium surface. Compared with conventional synthetic MOF films, the film prepared by this method is at least 16 times smoother (Fig. 9b), and the resulting ultra-smooth film can be used to form high-performance electrical connections that reduce the contact resistance by more than 13 times (Fig. 9c). They demonstrated the universality of this strategy by recreating the planes of nine distinct 2D c-MOF films with varying thicknesses (approximately 2–208 nm).

Hu *et al.* employed a polymer-assisted G–L interface technique to fabricate ultrathin Cu–HHTP films (Fig. 10a). Initially utilizing copper catecholate (Cu-HHTP)-comprising Cu ions and HHTP (HHTP = 2,3,6,7,10,11-hexahydroxytriphenyl)-as their C-MOF material allowed them to create an extensive super film on water's surface before transferring it onto quartz substrates.[76] The subsequent integration of nuclear metal molecular catalyst (DMC) and perovskite (PVK) quantum dots (QDs) into these Cu-HHTP films served as photosensitizers.

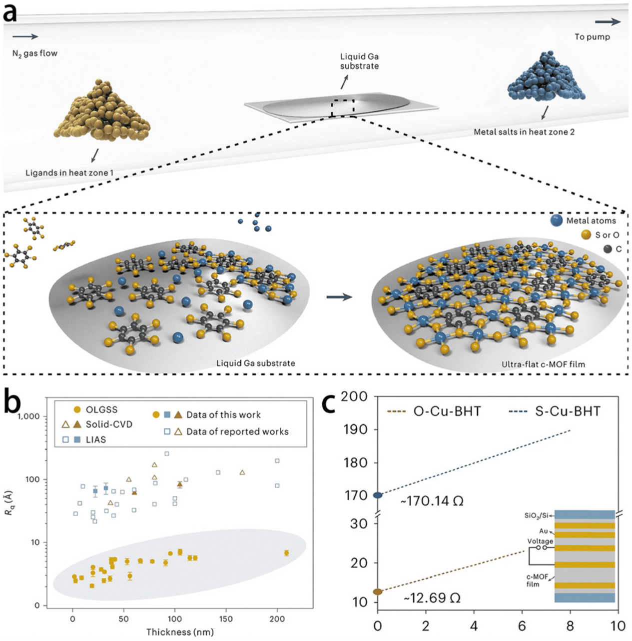

Fig. 9 (a) Diagrammatic representation of the preparation of 2D C-MOF films on different substrates. (b) Comparison of Rq of 2D c-MOF thin films obtained by OLGSS with those of previously reported MOF films in terms of film thickness. (c) Extrapolation of the fitted lines yields contact resistances of 12.96 Ω assigned to the OLGSS Cu-BHT film and 170.14 Ω assigned to the Cu-BHT film synthesized by traditional CVD method, suggesting an upgraded interface based on ultrasmooth OLGSS films. (Adapted from ref. 69 with permission from Springer Nature, Copyright 2024.)

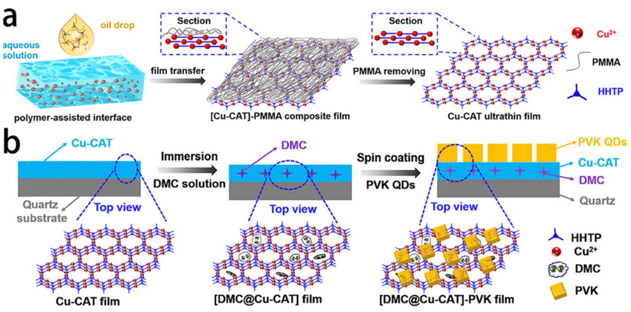

Fig. 10 (a) Scheme of the fabricating Cu-HHTP ultrathin film *via* the polymer-assisted gas–liquid interface strategy. (b) Fabrication process of [DMC@Cu-HHTP]–PVK composite film. (Adapted from ref. 70 with permission from American Chemical Society, Copyright 2024.)

Due to the combined steric hindrance effects and electrostatic interactions, the positively charged DMC infiltrated the anionic channels within the Cu-HHTP structure. Simultaneously, the negatively charged PVK became anchored to the positively charged membrane surface. The [DMC@Cu-HHTP]–PVK membrane prepared using the above steps can controllably integrate the catalytic and photosensitive centers (Fig. 10b).

2.3. Liquid–solid interface

It is usually necessary to transfer C-MOF films synthesized at the G–L interface or L–L interface to a conductive substrate (such as SiO_2/Si), aiming to manufacture (optoelectronic) electronic devices including sensors, photodetectors, field-effect transistors, and superconductors.[7,31,77] However, the transfer process can easily cause damage to the sample, thereby reducing device performance.[78] Compared with methods based on G–L and L–L interfaces, the L–S interface synthesis method enables direct thin film preparation on the target substrate, circumventing the need for additional transfer steps and thus promoting device integration.

The primary technique for growing MOF thin films on the L–S interface is layer-by-layer liquid-phase epitaxy (LBL-LPE), developed by Wöll and colleagues. This approach serves as a standard for MOF thin film preparation and can also be applied to deposit certain C-MOF films. One of the critical steps in using this strategy is functionalization of the substrate.[79,80] A common approach is to modify a layer of self-assembled monolayers (SAMs) on the substrate; the aim is to better anchor the metal center or organic ligand on the substrate surface for high-quality growth of the film.[81,82] The main advantage of SAMs is that the preparation process is convenient, and ultra-thin organic molecules can be arranged on various substrate surfaces by simple immersion. The most remarkable feature of the LBL is that the substrate does not need to be immersed in a mixed solution containing the reactants. Repeated contact with each precursor solution satisfied the condition of LBL cyclic growth, and the number of growth cycles could effectively control the thickness of the film.

For the first time, Xu's group used the LBL spray method to prepare high-quality C-MOF Cu-HHTP (HHTP: 2,3,6,7,10,11-hexa-hydroxytrimethylene) nanofilms (Fig. 11a and b).[83] The substrate was first pretreated in a piranha solution to obtain a hydroxylated surface, and then the copper acetate ethanol solution containing the metal precursor and HHTP ethanol solution containing the ligand precursor were alternately sprayed onto the surface of the functionalized substrate with nitrogen. After repeating the above process, the two precursors were epitaxially grown *via* LBL self-assembly to form a Cu-HHTP thin film. For every spraying process, the substrate was cleaned with ethanol to remove any unreacted precursor (Fig. 11a and b). The thickness of the film (20–100 nm) might be regulated by altering the quantity of cycles. The prepared Cu-HHTP thin films exhibited a dense arrangement, smooth surface, controllable thickness, excellent crystallinity, and electrical conductivity, approximately ten times greater than those of the corresponding powder samples.

Chen and colleagues reported a different LBL growth method by alternately immersing a functionalized target substrate in ethanol and an ethanol solution of reactants ($Cu(OAc)_2$ and HHTP ligand) (Fig. 11c–e).[84] A thickness-tunable fabrication of Cu-HHTP films was achieved through temporal modulation of the growth phase duration. This bottom-up synthetic strategy enables *in situ* electrochemical assembly of crystalline C-MOF films on current collectors, achieving angstrom-level precision in organic/electrode interfacial engineering while eliminating conventional transfer-induced contact resistance.

In 2021, Liu's team, drawing inspiration from capillary phenomena, introduced a face-to-face limited growth technique

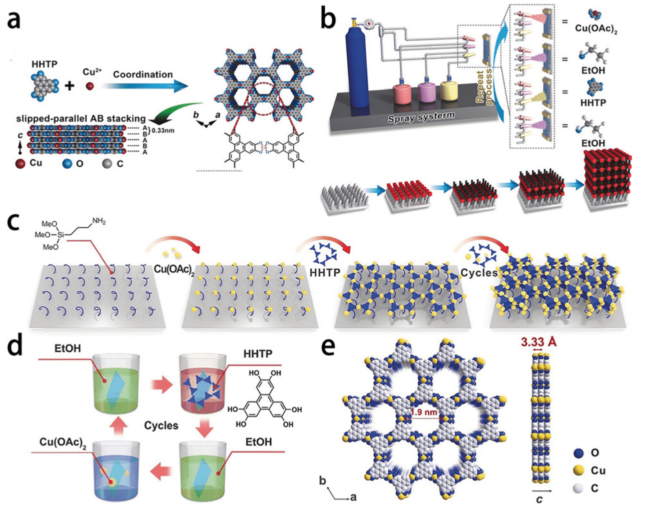

Fig. 11 (a) and (b) Schematic diagrams of the LBL self-assembly liquid-phase epitaxy spray method to fabricate Cu-HHTP thin films. (c) Illustration of the LBL growth procedure of the $Cu_3(HHTP)_2$ film on functionalized substrates and (d) repeated cycle growth. (e) Top and side views of $Cu_3(HHTP)_2$ proposed space-filling drawings in the slipped parallel stacking mode; hydrogen atoms are omitted for clarity. (Adapted from ref. 77 and 78 with permission from John Wiley and Sons, and John Wiley and Sons, Copyright 2017 and 2020, respectively.)

for fabricating two-dimensional Cu-TCPP films on dielectric substrates.[85] Capillary-driven microfluidic infiltration enabled autonomous delivery of sub-millimolar Cu^{2+} ions and TCPP) through continuous recirculation within the mesoporous electrode architecture, establishing a self-limiting reaction front that promotes directed molecular self-assembly while maintaining stoichiometric equilibrium. Initially, Cu^{2+} was anchored to the surface of the –OH-functionalized dielectric layer before reacting with the introduced TCPP ligand (Fig. 12a and b). Following the gradual removal of water molecules, the film was anchored to the surface of the dielectric layer. The conductivity of the Cu-TCPP MOF film is $\sim$0.007 S cm^{-1}, nearly ten thousand times higher than that of other carboxylic-acid-based MOFs. This methodology was applied to prepare other wafer-level C-MOF films, for instance M-HHTP (where M represents Cu, Co, and Ni).

The above are all single-oriented C-MOF thin films prepared by LBL-LPE. In 2023, Gu *et al.* used the LBL method to regulate the crystal planes of Cu-HHTP by adjusting parameters such as solvent, concentration, and temperature (Fig. 12c).[86] They conducted a more in-depth exploration of the nonlinear optical characteristics of Cu-HHTP films presenting diverse crystallographic orientations. The *z*-scanning technique was used to test these films. Results indicated that, at an unapplied voltage (0 V), the nonlinear absorption coefficient of the [001] oriented Cu-HHTP crystal film reached 7.6×10^{-6} m W^{-1}, while that of the [100] oriented Cu-HHTP crystal film was 8.4×10^{-5} m W^{-1}. This suggests that the [001] oriented Cu-HHTP crystal film exhibits significantly better nonlinear optical properties in the initial state than the [100] oriented Cu-HHTP crystal film. In addition, the nonlinear absorption properties of both crystalline films were enhanced when an external voltage was applied. With a gradual increase in the applied voltage, the nonlinear absorption coefficient of the [001] oriented Cu-HHTP film eventually increased to 3.84×10^{-5} m W^{-1}, while the [100] oriented Cu-HHTP film increased to 1.71×10^{-6} m W^{-1}.

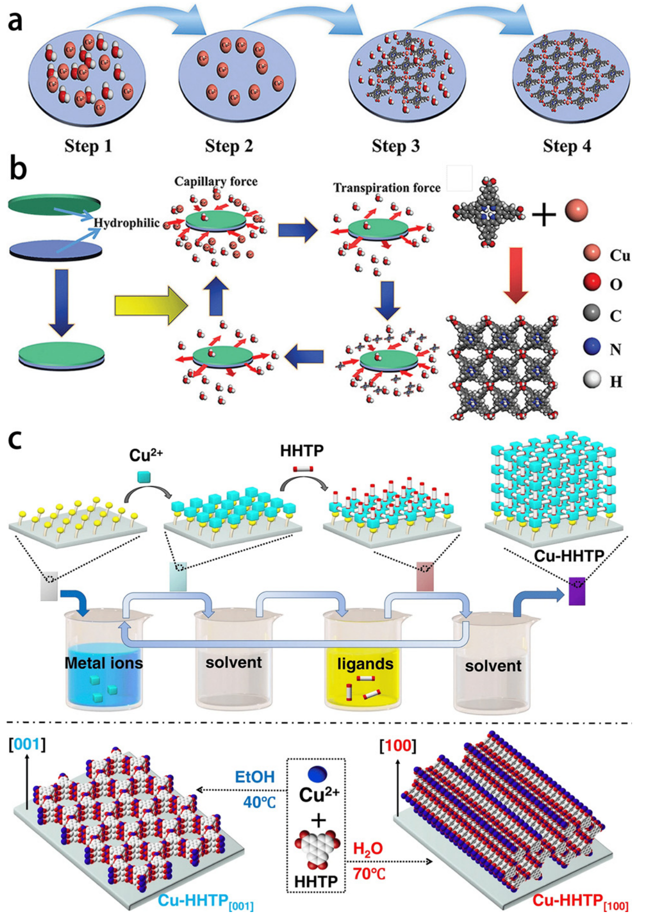

Fig. 12 (a) Schematic of the C-MOF film grown on dielectric substrates. (b) Schematic of coordination reaction between TCPP and Cu^{2+}. (c) Preparation of Cu-HHTP films with [001] and [100] orientations using the LPE LBL method. (Adapted from ref. 79 and 80 with permission from John Wiley and Sons, and Springer Nature, Copyright 2021 and 2022, respectively.)

2.4. Steam-assisted conversion method

Besides the L–S interface approach, the steam-assisted transformation method is likewise a thin film fabrication method capable of transforming into continuous crystalline thin films at suitable temperatures.

In 2021, Baldo *et al.* successfully developed Ni-HHTP thin films using an innovative two-phase solution–solid approach.[87] The core of this approach lies in the use of vacuum thermal vaporisation to deposit organic ligands as thin films onto silicon substrates. During the growth process, the reaction volume is skilfully confined within an elongated layer formed between two substrates, which are firmly bonded together by means of magnets. One of the substrates was in close contact with the ligand film, while the other formed an interface with a solid film of the metal salt precursor, which was completely submerged in a solvent and heated to a suitable temperature, resulting in the growth of Ni-HTP thin films on the substrate (Fig. 13a and b). Observations *via* SEM revealed that the crystal morphology obtained by this growth method was significantly different from that of the previously reported Ni-HTP needle-like crystals. This difference enabled the researchers to produce single-crystal wafers with lateral dimensions exceeding 10 μm, which are orders of magnitude larger than those produced by the previous method (Fig. 13c and d). In addition, the application of the gas-phase assisted conversion method further facilitated the growth of MOF films on the substrate, enabling the fabrication of self-supported C-MOF films and the ability to accurately control the thickness of the films to within 100 nm.

Utilizing the hydrophobic property of Ni-HITP, Hu *et al.* obtained centimeter-scale free-standing Ni-HITP thin films on the surface of an aqueous solution induced by alkaline vapor. Triethylamine existed independently in one of the containers as a basic vapor source, and the mixed solution containing metal and organic ligands as a precursor was placed in the same closed chamber as the essential vapor source without direct contact.[88] At 60 °C, the volatilization of triethylamine on the surface of aqueous solution leads to metal–organic coordination reaction to form the Ni-HITP film. The thickness could be controlled at 7–92 nm (Fig. 13e and f) according to the amount of the precursor. Notably, the choice of the fundamental steam source is very important in this process, and the high boiling point of *n*-propyl amine and solid basic ammonia are not conducive to film growth. Ni-HITP thin films floating on the liquid surface can be deposited on various substrate surfaces by the slow ''Fishing'' method for further study. As a new method for low-cost, large-area preparation of C-MOF films, the vapour-assisted technique is considered to have broad application prospects in future electrical devices and is expected to be an important breakthrough in the field of C-MOF film preparation.

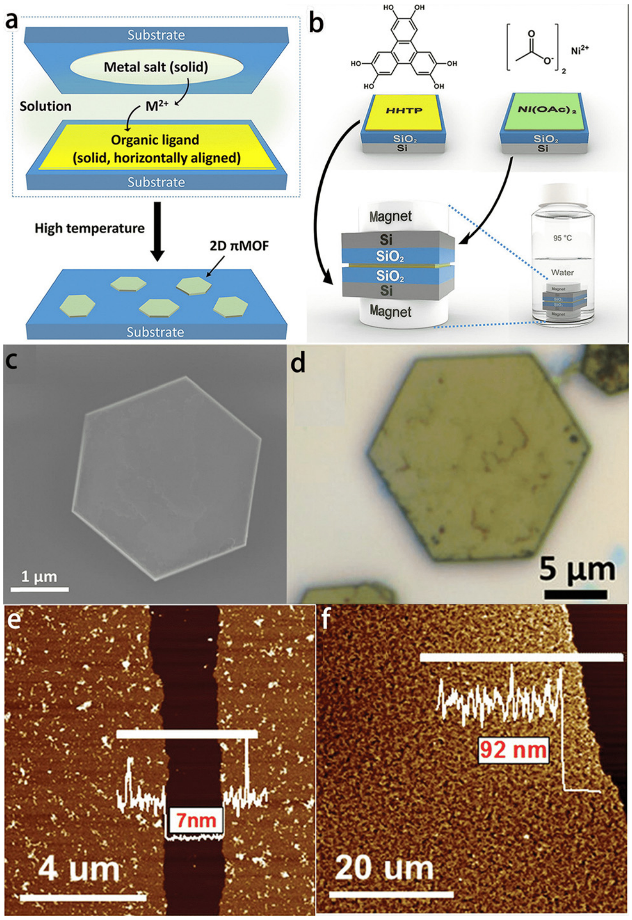

Fig. 13 (a) Schematic illustration of the solution-solid growth of C-MOFs. (b) Schematic of the growth method. The HHTP film was grown *via* vacuum thermal evaporation and $Ni(OAc)_2$ was drop-cast onto a separate substrate. (c) SEM image of Ni-HHTP crystals. (d) Optical microscope images of the crystal plates on a Si/SiO_2 substrate. (e) and (f) Topographic AFM and AFM height profile (inset) images of the 7 and 92 nm films. (Adapted from ref. 81 and 82 with permission from American Chemical Society, and John Wiley and Sons, Copyright 2021 and 2019, respectively.)

3. Investigation into the mechanisms of C-MOF thin film fabrication *via* interface-assisted techniques

The interface-assisted method offers numerous advantages for fabricating MOF thin films, and scientists are progressively elucidating the underlying film-forming mechanisms. Currently, the primary approaches for studying the growth process of thin films include grazing incident XRD,[89,90] quartz crystal microbalance (QCM),[90,91] AFM,[92] SEM,[89] and spectroscopy.[91,93]

WÖll's team has achieved significant results in the field of film formation mechanisms by interface-assisted methods, and in 2007, they used an innovative synthetic strategy to synthesize Cu-BTC (Cu-based benzene tricarboxylic acid), a metal–organic framework (MOF) material, in the reverse order of the previous synthesis scheme by means of a repetitive immersion cycle, thus providing an in-depth insight into its synthesis mechanism.[94] This unique synthesis method used not only successfully achieved the preparation of highly crystalline and homogeneous Cu-BTC MOF films (Fig. 14a), but also opened a new path for the development of novel ordered MOF structures. Simultaneously, the LBL approach offered a distinctive chance to develop novel MOF-ordered architectures composed of alternating strata, possibly with non-periodic configurations of diverse metal ions and/or various linkers.

The team then used scanning force microscopy to study MOFs selectively fabricated on carboxyl-functionalized surfaces and to validate the effectiveness of the stepwise preparation method and its ability to prepare high-quality surface metal–organic structures. The thickness and planarity of the synthesized MOF films were examined through the characterization of specimens with varying numbers of cycles (Fig. 14b and c).[95] The number of layers deposited was proportional to the quantity of immersion cycles. This suggests that upon the initial nucleation of the Cu-BTC layer within the COOH terminal domain, all the ensuing substances were integrated into the pre-nucleated layers. Thus, it was confirmed that sequential

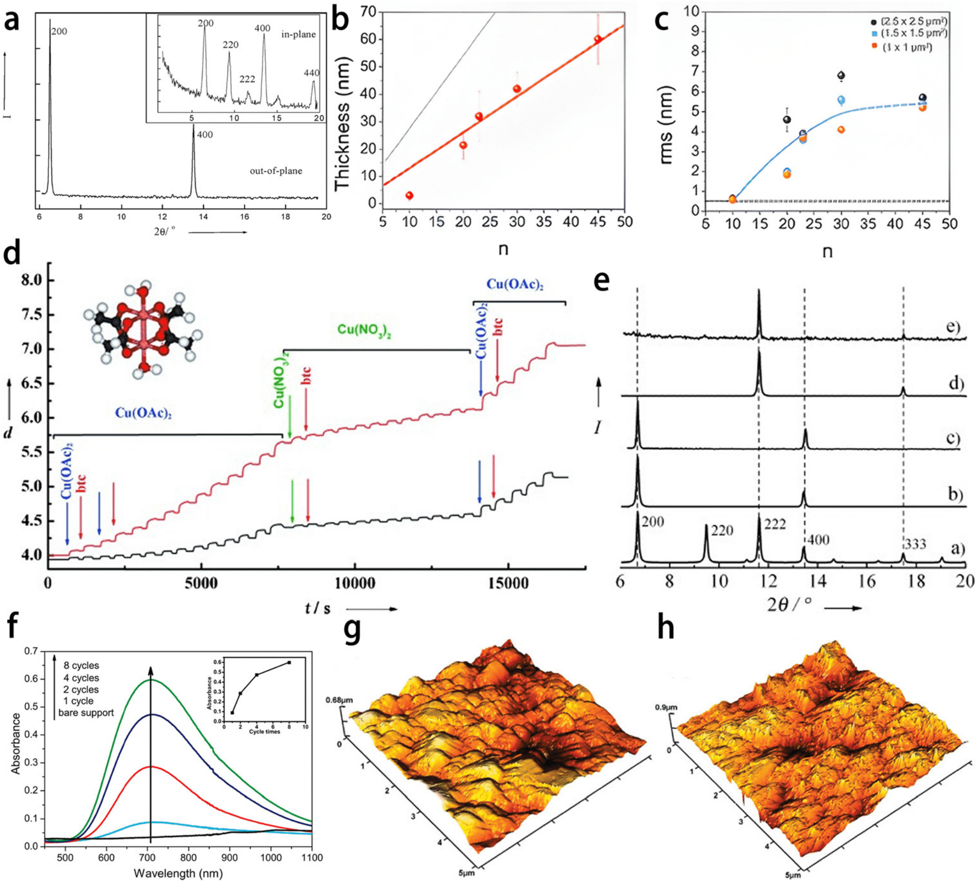

Fig. 14 (a) XRD pattern of Cu-BTC film. (b) The functional relation between film thickness and growth cycle number. (c) Root mean square (RMS) surface roughness as a function of number of immersion cycles calculated for different scan sizes. (d) The SPR signal recorded as a function of time. (e) Out-of-plane XRD data for Cu-BTC. (f) Ultraviolet-visible absorption spectra of alumina support after step-by-step seeding for various numbers of cycles; inset shows the absorbance *versus* number of cycles at 714 nm. (g) AFM images of the bare and (h) step-by-step seeded supports after four cycles. (Adapted from ref. 87–90 with permission from American Chemical Society, Royal Society of Chemistry, Royal Society of Chemistry, and American Chemical Society, Copyright 2007, 2008, 2009 and 2011, respectively.)

growth to thicker films could be followed, which promises to build high-quality 3D structures based on laterally confined MOF. Immediately following the *in situ* SPR monitoring of the stepwise formation of MOF, a new mechanistic study of the nucleation and growth of MOF and the formation of SBUs was carried out by investigating the deposition of selected building blocks separately (Fig. 14d).[96] XRD data analysis showed that on the OH-terminated surface, the MOF layer grew along the [111] direction. Conversely, on the COOH-functionalized surface, Cu-BTC growth occurred along the [100] direction (Fig. 14e). Thus, the organic surface acts as the nucleus for MOF growth and controls the MOF growth direction.

Based on the above research foundation, in 2011, Nanping Xu's research group deeply analysed the growth process of Cu-BTC thin films using UV-Vis spectroscopy.[93] In the experiment, the researchers found that the maximum absorption peaks of all the samples were located at about 714 nm (Fig. 14f), and this absorption peak was highly consistent with the characteristic absorption peaks of Cu-BTC samples. This indicates that the chemical structure of the Cu-BTC film remained stable during the growth process, and its characteristic absorption peak could be used as an important indicator for monitoring the growth state of the film. To further investigate the microstructural changes in the films at different growth stages, AFM was employed to observe the morphology of the implanted scaffold surface in detail. As the number of cycles increased, AFM images showed that the morphology of the scaffold surface gradually changed. At the early stage of growth, sparse spikes corresponding to Cu(II) carboxylic acid complexes can be identified (Fig. 14g and h), which suggests that the growth of the Cu-BTC film starts from these sparsely distributed complexes. With increasing number of cycles, the number of these spikes gradually increased, indicating that the coverage of the film gradually increased, and the growth process gradually tended to be complete. This microstructural change corroborates the results of UV-Vis spectroscopic analysis, providing a more comprehensive understanding of the growth mechanism of Cu-BTC films.

In 2012, Allendorf *et al.* used a QCM electrode to study MOF thin film formation kinetics and mechanisms *in situ*.[97] They thoroughly investigated the various factors affecting the stepwise growth process of Cu-BTC and revealed the characteristics of its mechanical behavior during the growth process. In addition, they confirmed that the film formation is a thermally driven process, and its reaction rate is closely related to the temperature, which is significantly accelerated with the increase of temperature, which provides an important basis for understanding the kinetic mechanism of film growth (Fig. 15a and b). In addition, they found that the growth rate of MOF films varies depending on the composition of the substrate surface in the following order: alumina surface > silicon oxide surface > hydroxyl self-assembled single molecule film (OH-SAM) surface > carboxyl self-assembled single molecule film (CO_2H-SAM) surface (shown in Fig. 15c). Using real-time, *in situ* monitoring of the MOF growth process through frequency and dissipation measurements, the researchers obtained key data on the film growth kinetics, which provided a solid and reliable basis for subsequent calculations related to the reaction rate as well as transition state thermodynamics. Based on these findings, they finally proposed a comprehensive and systematic mechanism for the formation of MOF films (Fig. 15d).

In 2014, Terfort's team[98] conducted a highly significant study. They utilized infrared reflection absorption spectroscopy (IRRAS) in combination with advanced characterization techniques such as X-ray diffraction (XRD) and scanning electron microscopy (SEM) to delve into the growth characteristics of $[Cu_2(F_4bdc)_2(Dabco)]$ metal–organic framework (MOF) thin films grown on carboxylate and pyridine-terminated surfaces *via* the layer-by-layer (LBL) method. Here, Dabco represents 1,4-diazabicyclo[2.2.2]octane, and F_4bdc represents terephthalic acid with four fluorine atoms. During the research, they discovered that achieving complete oriented deposition of MOF thin films hinges on selecting the appropriate surface chemical composition and temperature. Specifically, when the carboxylate acts as the terminal surface, the desired [100]-oriented MOF thin film can be successfully obtained at low temperatures, particularly at 5 °C (as shown in Fig. 16a–c). This growth process at low temperatures allows the MOF thin film to grow along a specific crystallographic direction, thereby achieving a highly oriented structure. In contrast, when the surface is terminated with pyridine, the predicted [001]-oriented MOF film can only be obtained at a higher deposition temperature of 60 °C (as shown in Fig. 16a, b and d). This indicates that different surface chemical environments and temperature conditions have a significant impact on the growth orientation of MOF thin films.

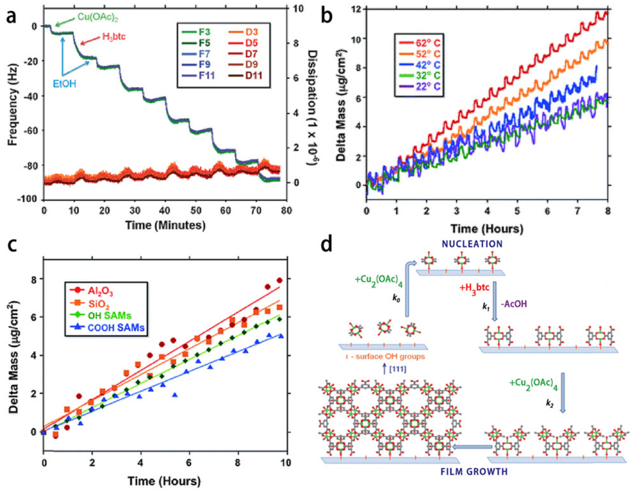

Fig. 15 (a) QCM-D plot depicting the alterations in harmonic frequencies and dissipation of the fifth $Cu(OAc)_2$-H_3btc subsequent to its deposition on silicon dioxide-coated electrodes at 15 °C. Flow rate: 100 mL min^{-1}. (b) Temperature-dependent studies of Cu-BTC deposition on alumina- and silica-coated substrates (c) Cu-BTC deposition on aluminium oxide, Au, and silicon dioxide functionalized with OH and COOH functional group at 32 °C. (d) Schematic illustration of the put – forward model for Cu-BTC nucleation and growth on oxide surfaces. The atoms are presented as follows: C, gray; O, red; and Cu, green. (Adapted from ref. 91 with permission from Royal Society of Chemistry, Copyright 2012.)

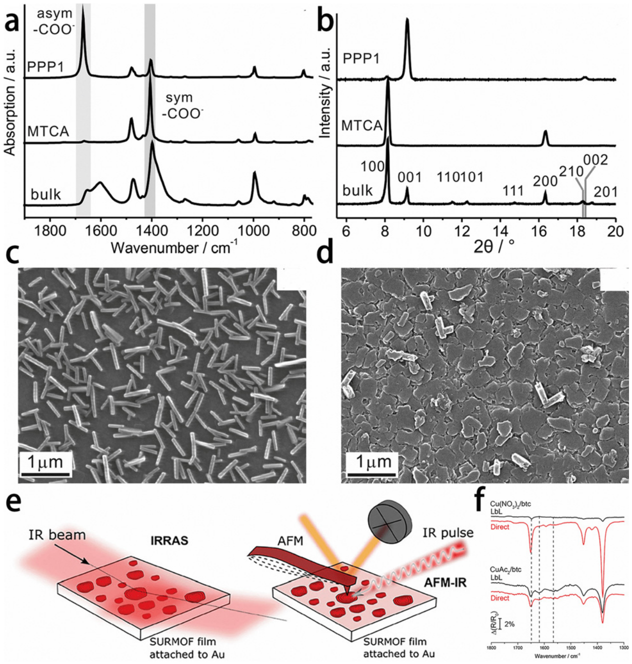

Fig. 16 (a) IRRA spectra, (b)SXRD spectra, and (c) and (d) SEM images of $[Cu_2(F_4bdc)_2(dabco)]$ MOF film-directed LBL growth on two different SAM (PPP1 and MTCA). (e) Schematic of the working principles of IRRAS and AFM-IR techniques. (f) Comparison of IRRAS spectra of Cu-BTC films obtained after three cycles of manual synthesis, with full cycle drying steps (black), and after the subsequent addition of the reactant mixture overnight (red), copper nitrate (top), and copper acetate (bottom). (Adapted from ref. 92 and 85 with permission from Springer Nature, American Chemical Society, and John Wiley and Sons, Copyright 2015 and 2024, respectively.)

In 2017, Bert and colleagues used a combination of AFM-IR imaging and infrared reflectance absorption spectroscopy (IR) to investigate the effect of the concentration of the secondary building unit (SBU) solution on the MOF film growth mechanism (Fig. 16e).[91] When the MOF films were grown according to a manual procedure for three immersion cycles and then soaked in a direct synthetic solution (namely, a solution encompassing the BTC linker and the Cu precursor) overnight, a much faster growth rate of the $Cu(NO_3)_2$-derived MOF films was observed (Fig. 16f top). This presents a contrast to an analogous substrate positioned within a direct synthesis solution encompassing the $CuAc_2$ precursor, which demonstrated merely LbL deposition and no time-dependent delayed MOF film synthesis *via* SBUs in the solution (Fig. 16f bottom).

Anderson's team investigated the film formation, porosity, and transport properties of MOF-399 and MOF-14 films using AFM and electrochemistry at this time.[92] AFM disclosed the unblemished film morphologies of the MOF-399 and MOF-14 systems. The surface roughness was governed by the substrate, and the films exhibited linear growth rates of 1.4 and 2.2 nm per layer, respectively (Fig. 17a and b). The electron transport characteristics of the films were assessed through electrochemical impedance spectroscopy. It was determined that MOF-399 film was electronically non-conducting, and the MOF-14 film exhibited low electronic conductivity (Fig. 17c and d). The intrinsic porosities of these ultrathin MOF mimetic films were characterized using a ferrocene cyclic voltammetry redox probe. The peak currents of the MOF-399 mimetic membranes were larger than those of the MOF-14 membranes, which is consistent with the higher porosity of MOF-399 (Fig. 17e and f).

Kind's team then investigated the effect of reactant solution concentration on the *in situ* growth of $Cu_2(F_4bdc)_2$ (dabco) MOF thin film (where F_4bdc represents tetrafluorobenzene-1,4-dicarboxylate and dabco denotes 1,4-diazabicyclo[2.2.2]octane), using a QCM, *in situ* spectroscopic, diffractive, and microscopic techniques.[89] By systematically varying the reactant concentrations, a strong effect on the growth mechanism was found, leading to different densities, sizes, and morphologies of MOF crystals, with high reactant concentrations providing a large number of crystalline nuclei in the initial stages of the LbL cycle, and minor concentrations limiting the amount of deposited MOF material in the later stages of the LBL process (Fig. 18a).

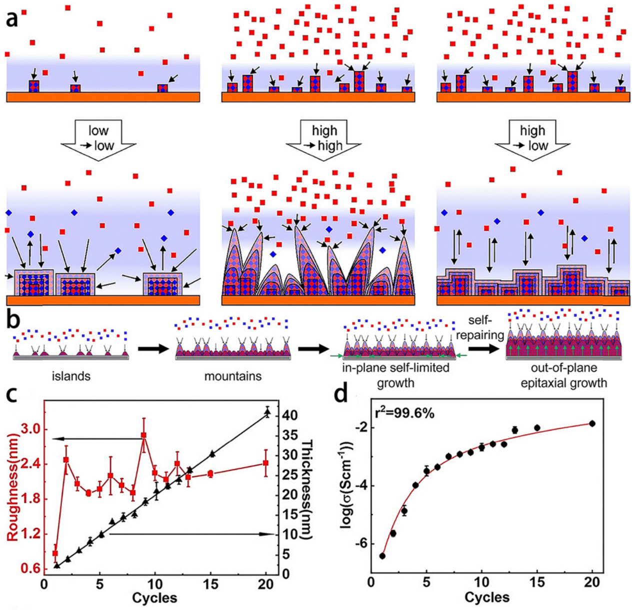

Fig. 18 (a) Scheme of the mechanism of concentration-dependent MOF film deposition. (b) Schematic of Cu-HHTP-xC growth mechanism. (c) Growth cycle relationship of thickness and roughness of Cu-HHTP-xC. (d) Voltage curve of Cu-HHTP-xC. (e) Growth cycle correlation log curve for Cu-HHTP-xC. (Adapted from ref. 83 and 93 with permission from John Wiley and Sons, and John Wiley and Sons, Copyright 2020 and 2022, respectively.)

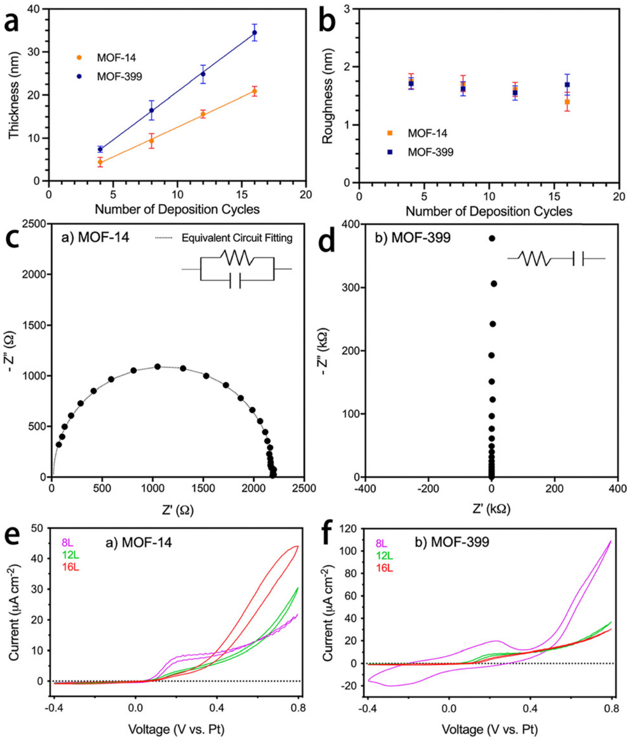

Fig. 17 (a) MOF film thickness and (b) roughness determined by AFM. (c) Representative EIS spectra of the 8 L MOF-14 and (d) 12 L MOF-399-based films. (e) Porosity of 8, 12, and 16 L of MOF-14- and (f) MOF-399-based films in 10 mM Fc|100 mM TBATFB PC at a sweep rate of 10 mV s^{-1}. (Adapted from ref. 86 with permission from American Chemical Society, Copyright 2019).

Building upon the preceding exploration of the formation mechanisms of MOF films, Xu's team selected Cu-HHTP, a C-MOF film, as a representative case to investigate the underlying principles of LBL-LPE technology and elucidate its growth mechanism characterized by 'in-plane self-limiting and self-healing' (Fig. 18b).[99] The orientation, structural defects, and grain boundaries of Cu-HHTP-XC films were examined through microanalysis and electrical measurements. Notably, the growth cycles did not significantly alter the surface morphology of Cu-HHTP; the average roughness remained stable at approximately 2.2 nm with minimal fluctuations (Fig. 18c). The thickness of the film increased uniformly at an average rate of approximately 2 nm per cycle. By using the two-electrode method to precisely measure the *I–V* (current–voltage) curve, this measurement method not only reveals the law of conductivity change with the increase of film thickness, but also provides key data for optimizing the electrical properties of the film (Fig. 18d). These C-MOF films are synthesized directly at the liquid/solid interface using a LBL approach.

4. Applications

Owing to their intrinsically high electrical conductivity and distinctive properties, including precisely defined pore size, distinct active sites, and large specific surface area, C-MOFs have demonstrated potential in optoelectronic and electronic devices. The successful fabrication of thin films confers the benefits of facile processing and integration of C-MOFs.

4.1. Field-effect transistors

Field-effect transistors (FETs) are unipolar devices controlled by charge carriers and regulated by gate voltage. They offer low noise, low power consumption, high input impedance (10^8–10^9 Ω), wide dynamic range, no secondary breakdown, easy integration, and a broad safe operating area, making them strong competitors to bipolar and power transistors.[100] FETs control current between the source and the drain using the gate voltage. C-MOF thin films, with their ordered crystalline structures, tunable charge transfer channels, adjustable band structures, and versatile preparation methods, are promising candidates for FET active channels.[80,101]

In 2017, Xu *et al.* successfully synthesized Ni-HITP thin films on the G–L interface for the first time, obtaining high-quality Ni-HITP thin films. After stamping transfer, the thin films with a smooth surface were transferred to a SiO_2/Si substrate to prepare microporous FET devices, constructing bottom-gate field-effect transistor devices with top contact geometry (Fig. 19a).[71] The Ni-HITP thin film, when used as a functional layer in FET devices, demonstrated characteristic p-type semiconductor properties. It achieved a switching ratio as high as 2×10^3 and exhibited a carrier mobility of 48.6 $cm^2\ V^{-1}\ s^{-1}$ (Fig. 19b and c). To improve the interface quality between the active layer and substrate of C-MOF thin films, Duan's team designed a method of *in situ* growth of large-area and uniform Ni-HITP thin films at the L–S interface to fabricate Ni-MOF FETs.[102] The device has a switching ratio of 2.29×10^3 and a mobility of 45.4 $cm^2\ V^{-1}\ s^{-1}$. Additionally, they fabricated a Ni-HITP-based liquid-gate FET device, using phosphate-buffered saline as the liquid gate (Fig. 19d–f).

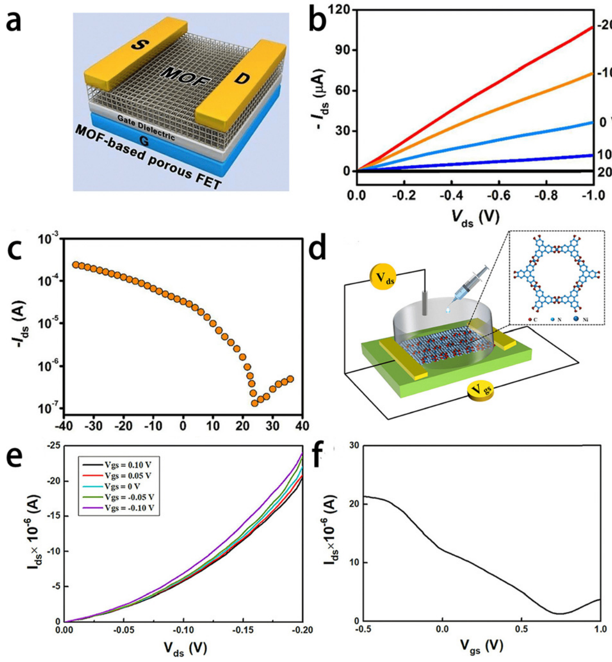

Fig. 19 (a) Schematic of the FET structure based on a thin Ni-HITP film. (b) I_{ds} *versus* V_{ds} output curves and (c) I_{ds} *versus* V_{gs} transfer curve of the device. (d) Scheme of the liquid-gated FET device structure based on the $Ni_3(HITP)_2$ thin film with phosphate-buffered saline as the liquid gate. (e) I_{ds} *vs.* V_{ds} output curves and (f) I_{ds} *vs.* V_{gs} transfer curves of the FET device. (Adapted from ref. 64 and 96 with permission from American Chemical Society, and American Chemical Society, Copyright 2017 and 2019, respectively.)

4.2. Chemiresistive sensors

Chemiresistive sensors are widely used in environmental detection, indoor air quality detection, and other fields due to their portability and fast response speed. Unlike other types of gas sensors, the basic working principle is the change in the resistance value with the absorption of the target gas; thus, it has the advantages of simplicity and easy control. Therefore, C-MOF materials with ultrahigh specific surface areas and adjustable pore structures are an ideal class of gas-sensing materials. So far, most C-MOF gas sensors are powder or thick film types, which seriously affect gas and electron transfer in the device.[103,104] To improve the gas sensing performance of such C-MOF electronic devices, the controllable preparation of high-quality C-MOF nanofilms is essential.[105]

In 2017, Xu's group achieved the first self-assembly of high-quality Cu-HHTP nanofilms (20–100 nm) based on redox-active ligands on hydroxy-functionalized substrate surfaces.[83] Cu-HHTP thin film sensors exhibited excellent room temperature NH_3 sensing performance and p-type semiconductor characteristics compared to corresponding thick film devices. The film with a thickness of 20 nm showed the best performance for detecting NH_3, exhibiting a high response value, high selectivity, fast response speed (response time of 1.36 min), and good stability (response value remained at 88% after 3 months) (Fig. 20a). The team also used spray-assisted LBL self-assembled liquid-phase epitaxy to obtain HITP-doped Cu-HHTP nanofilms (20–70 nm).[106] Due to the defects caused by HITP doping, the selectivity of benzene vapor for ammonia was improved by more than 220% (Fig. 20b).

However, the C-MOF films mentioned above are limited by their small exposure areas and slow charge transfer. To address this issue, Xu and colleagues designed an LBL self-assembly strategy for growing Cu-HHTP 3D thin films on the surface of metal–oxide nanowires. They obtained Cu-HHTP 3D nanofilm chemiresistive gas sensor components. Compared to the corresponding Cu-HHTP 2D film, the Cu-HHTP 3D film optimized the detection limit of ammonia gas by 1000 times at room temperature, increased the response value by 250% (0.7 mg m^{-3}), and increased the response speed by 130%, providing a novel approach for the formation of C-MOF films on nanostructured substrates (Fig. 19c).[107] The device is sensitive to small changes in environmental CO_2 concentration within the 400–1000 ppm range.

4.3. Optoelectronic devices

Optoelectronic devices are made based on the photoelectric effect and are also known as photosensitive devices.[108] There

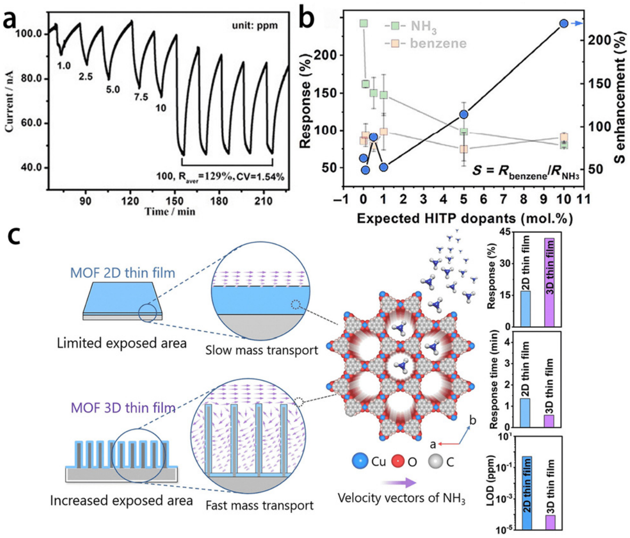

Fig. 20 (a) The response–recovery curve of Cu-HHTP thin films toward NH_3 with different concentrations. (b) Response recovery time curves of HITP-doped Cu-HHTP nanofilms toward 100 ppm NH_3 response–concentration log–log plots. (c) Comparison of Cu-HHTP 3D and 2D films. (Adapted from ref. 77, 102 and 103 with permission from John Wiley and Sons, Springer Nature, and John Wiley and Sons, Copyright 2017, 2020 and 2021, respectively).

are many optoelectronic devices, but their working principles are based on the physical foundation of the photoelectric effect. The main types of optoelectronic devices include phototubes, photomultiplier tubes, photoresistors, photodiodes, *etc.*[51]

In 2020, Feng's group developed devices based on a semiconductor Fe-HTTP thin film of double-ended photodetectors.[109] An Fe-HTTP film was deposited on a glass substrate, with indium serving as the electrode. This photodetector demonstrated a broad optical response, capable of detecting wavelengths spanning from ultraviolet to near-infrared regions (ranging from 400 to 1575 nm) (Fig. 21a–d). Compared with the results at room temperature, the photodetector performance at 77 K improved significantly. After cooling, the performance of the device improved, including improving the specific detection rates, optimizing the noise-equivalent power, and enhancing the photosensitivity and voltage response. At 77 K, for the current–voltage curves of 785 nm laser-irradiated devices under different power densities, the photocurrent rose with increasing photon density (Fig. 21e). Temperature-reliant photosensitivity assessments were conducted within the temperature interval of 77–300 K to clarify the influence of temperature. The results show a negative correlation due to the narrow infrared band gap of the Fe-HTTP films. In general, narrow bandgaps facilitate the thermal generation of free carriers at room temperature (Fig. 21f). In contrast, decreasing temperatures diminish the thermally activated inter-band population, thus enhancing the optical detection performance. At 77 K, the response time was 2.3 s during the ascending process and 2.15 s during the descending process.

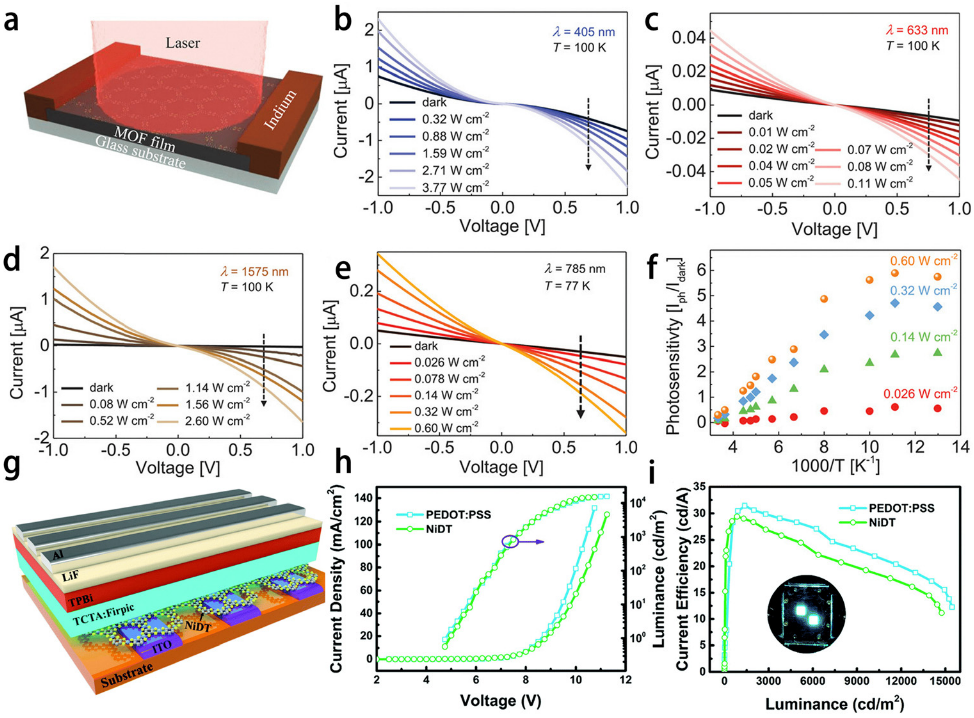

Fig. 21 (a) Schematic illustration of two-terminal photodetector device based on Fe-HTTP thin films. (b) Current–voltage curves of the device after exposure to a 785 nm laser with varied power densities at 77 K. (c) Temperature-dependent photosensitivity of the device illuminated by varying light strength. (d)–(f) Photoresponses of the MOF detector at 100 K at 405 nm (d), 633 nm (e), and 1575 nm (f). (g) Schematic illustration of blue small-molecule OLED based on Ni-HTB thin films. (h) Voltage-dependent current density and luminance characteristics of the devices. (i) Luminance-dependent current efficiency characteristics of the devices. (Adapted from ref. 106 and 107 with permission from John Wiley and Sons, and Royal Society of Chemistry, Copyright 2020 and 2020, respectively.)

Nishihara *et al.* constructed organic light emitting diode (OLED) devices using a $Ni_3(HHTP)_2$ C-MOF film as a hole-buffer layer.[110] A synthetic l-interfacial $Ni_3(HHTP)_2$ film was transferred onto an ITO glass substrate for OLED integration. Compared to traditional OLED devices, OLED devices fabricated with C-MOFs have better stability (Fig. 21g–i). Wang and his team utilized the excellent optical transparency (82%), superior electrical conductivity (2500 S cm^{-1}), and easy solution-processability of Cu-HTB thin films for transparent electrodes in solar cells. The performance of Cu-HTB solar cells is comparable to that of traditional ITO electrode functional devices.[111]

4.4. Others

4.4.1. Electrochemical sensors. Electrochemical biosensors are favored because of their low cost, short analysis time, convenient operation, high sensitivity, and real-time detection.[112] Electrochemical sensors consist of at least two components, a receiver and a sensor, which interact with the analyte (the recognition layer), and the sensor converts the information into an electrical signal. Most electrochemical sensors are based on potential or current measurements, and Coulomb devices are used for specific applications.[113] The commonly used electrochemical methods include electrochemical impedance spectroscopy (EIS), differential pulse voltammetry (DPV), square wave voltammetry (SWV), cyclic voltammetry (CV), and chronoamperometry. C-MOFs have unique structures and properties, such as excellent conductivity and high stability, with great application prospects in electrochemical sensing.[114–116]

Liu *et al.* obtained Cu-BHT thin films (thickness <20 nm) along the (001) orientation, in which the upper surface was smooth and the lower surface was island-shaped.[117] The films exposed on the upper and lower surfaces could be made into microchip electrochemical sensors for detecting H_2O_2, but their sensing performances were different (Fig. 22a and b). Both experimental studies and theoretical calculations consistently show that the insulating film with the lower surface exposed exhibits more crystal defects as well as a larger interfacial area due to its unique structural features. These properties enable the film to provide more active sites and reaction channels when interacting with H_2O_2 (hydrogen peroxide) molecules, which significantly enhances the sensing performance for H_2O_2.

In 2022, Mirica *et al.* prepared (001)-oriented and (100)-oriented M-HHTP MOFs *via* epitaxially controlled deposition of M-HHTP MOFs (M = Ni, Co) on electrodes.[118] The electrochemical characterization techniques were employed to determine the contributions of the base ([001] plane) and edge sites ([100] plane) in these MOFs. Despite the low rate constant of heterogeneous electron transfer observed, the [001] surface of M-HHTP exhibited greater sensitivity and selectivity for dopamine detection compared to the [100] surface. The low detection limit (LOD) in phosphate-buffered saline was 9.9 ± 2 nm; in simulated cerebrospinal fluid, it was 214 ± 48 nm (Fig. 22c and d).

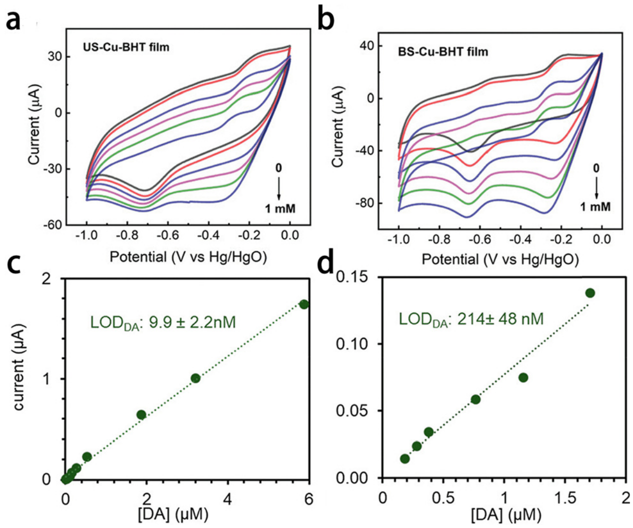

Fig. 22 Cyclic voltammograms of (a) US-Cu-BHT and (b) BS-Cu-BHT films at different concentrations (0–1 mmol L^{-1}) of H_2O_2. (c) and (d) Sensitivity of Ni-HHTP for DA detection using differential pulse adsorption stripping voltammetry (DPASV) in each analytical solution. (c) DPASV traces of increasing [DA] in 0.1 M PBS. (d) DPASV of DA in a simulated cerebrospinal fluid (CSF) solution containing UA, glucose, and 0.5% bovine serum albumin. (Adapted from ref. 114 and 115 with permission from American Chemical Society, and John Wiley and Sons, Copyright 2021 and 2022, respectively.)

4.4.2. Capacitor. With the intensification of environmental and energy issues, C-MOF thin films find extensive energy – related applications attributable to their distinctive structure, substantial specific surface area, and tunable porosity. A capacitor consists of two electrodes and the dielectric substance between them.[119] A dielectric material belongs to a category of dielectrics. When it is situated within an electric field formed between two parallel plates bearing equal magnitudes of opposite electric charges, polarization occurs within the dielectric. As a result, polarization charges are induced on the surface of the dielectric. This induction process leads to an increment in the charge bound to the plates, all the while keeping the potential difference between the plates constant.[120] This is the reason why capacitors possess capacitive properties. The capacitance, the area of the plates, and the permittivity of the dielectric materials ε are directly proportional and inversely proportional to the thickness of the dielectric material (that is, the distance between the plates). So, preparing thinner C-MOF films can increase the capacitance of capacitors.[121–123]

In 2017, Dincă *et al.* first employed Ni-HITP powder as an active electrode material for electrochemical double-layer supercapacitors.[124] However, due to the gaps formed by powder accumulation hindering ion transport at high current densities, the rate performance of the capacitor was poor. In 2021, Zhao *et al.* utilized a LBL self-assembly method to obtain ultra-thin Cu-HHTP films on ITO/PET substrates and applied them to flexible transparent conductive electrodes (FTCEs) and flexible transparent supercapacitors (FTSCs) Cu-HHTP/ITO/PET FTCEs exhibit excellent electrochemical performance (area capacitance CA = 1700 μF cm^{-2}) and optoelectronic properties (resistance Rs = 49.1 Ω sq^{-1}, transmittance T550 nm = 82.2%).[125] At a current density of 7 μA cm^{-2}, the area capacitance can reach 939.2 μF cm^{-2}

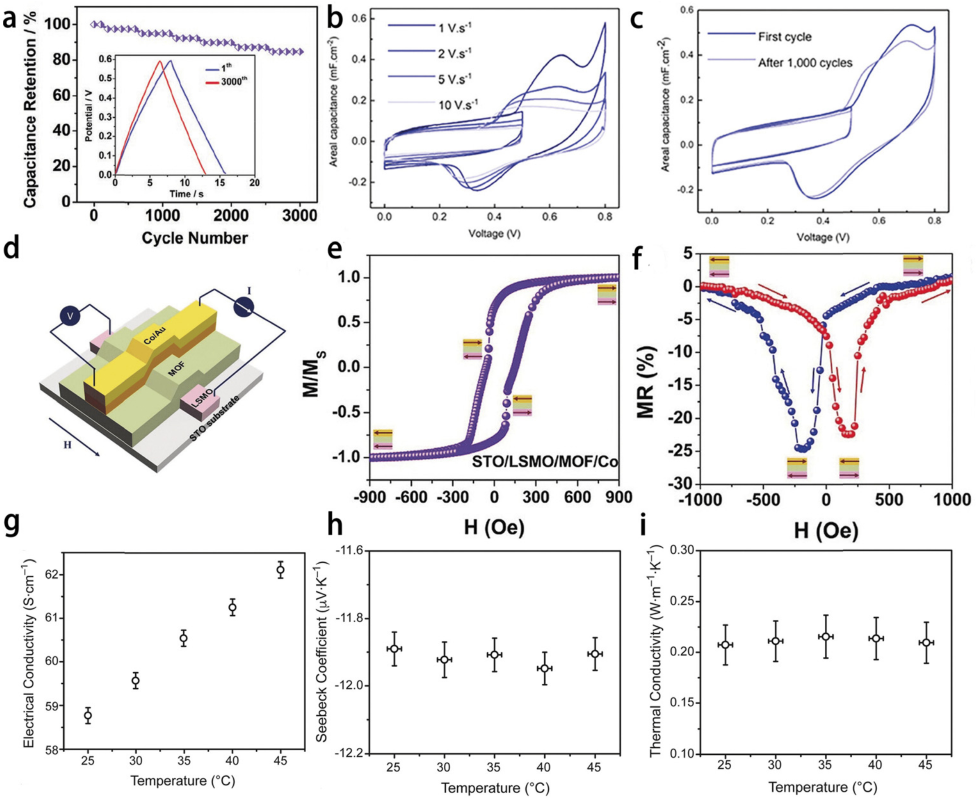

Fig. 23 (a) Cycling performance measured at a current density of 70 μA cm^{-2} (inset: GCD curves at 1st and 3000th cycles). (b) Cyclic voltammograms of Ni-HITP micro-supercapacitor in 1 M KOH aqueous electrolyte at different scan rates. (c) Cyclic voltammograms at a scan rate of 5 V s^{-1} showing the stability of the device over 1000 cycles. (d) The C-MOF-based vertical OSVs with schematic diagram. (e) Magnetic hysteresis loops and (f) MR loop for LSMO/Cu3(HHTP)2 (100 nm)/Co OSVs at 10 K. (g) Seebeck coefficient of Ni-HITP. (h) Thermal conductivity of Ni-HITP. (i) Thermoelectric figure of merit. (Adapted from ref. 122, 123, 78 and 128 with permission from John Wiley and Sons, John Wiley and Sons, John Wiley and Sons, and Elsevier, Copyright 2021, 2024, 2020 and 2020, respectively.)

in 3000 cycles, and the performance can maintain 85% of the original, with good mechanical flexibility (Fig. 23a). Vlad's team recently achieved uniformly crystallized Ni-HITP films through non-sacrificial anode deposition and utilized them in miniature supercapacitors.[126] Utilizing cyclic voltammetry and 1.0 M potassium hydroxide as the electrolyte, the Ni-HITP miniature supercapacitor demonstrates a pure double-layer capacitor storage mechanism with an average area capacitance of 0.27 mA cm^{-2} within a finite voltage range of 0–0.5 V (Fig. 23b). After 1000 cycles at a sweep rate of 5 V s^{-1}, no significant change in capacitance (at voltage windows of 0–0.5 V and 0–0.8 V) was observed, indicating the stability of the device (Fig. 23c).

4.4.3. Spin valve.

Organic spin valve is a new type of spintronic device, which shows great potential for applications in quantum computing, data storage and other fields.[17,127] The basic structure of an organic spin valve usually consists of a ferromagnetic (free) layer/non-magnetic layer/ferromagnetic layer/antiferromagnetic layer (pinned layer). This structure is similar to a sandwich, and under the action of an applied magnetic field, the device demonstrates a low-resistance state when the magnetization orientations of the ferromagnetic electrodes on both ends are aligned in parallel. In contrast, it shows a high-resistance state when the magnetization orientations are aligned in an anti-parallel configuration. In 2019, Feng's team selected LBL self-assembly oriented C-MOFs thin film $Cu_3(HHTP)_2$ grown on $La_{0.67}Sr_{0.3}MnO_3$(LSMO)FM electrode as an organic space layer to construct an organic spin valve (Fig. 23d–f). This LSMO/Cu-HHTP/Co spin valve achieves a magnetoresistance of 25% at 10 K. This achievement not only demonstrates the excellent performance of organic spin valves at low temperatures, but also provides an important experimental basis for future applications in fields such as quantum computing and data storage.[84]

4.4.4. Thermoelectricity.

Thermoelectricity refers to the phenomenon of charge generation in various crystals due to temperature changes.[128] The Seebeck effect refers to the thermoelectric phenomenon caused by the temperature difference between two different electrical conductors or semiconductors, which results in a voltage difference between the two materials.[129,130] This phenomenon does not only reveal the direct conversion between heat and electricity. The core of the Seebeck effect resides in the contact potential disparity between two metals, which is contingent upon the two essential elements of the metal's electron escape work and effective electron density. In addition to being widely used in optoelectronic devices, C-MOFs have promising applications in the thermoelectric field.[131,132] Dinca *et al.* studied the thermoelectric properties of Ni-HITP films. They found that the Ni-HITP film is a typical n-type thermoelectric material, which exhibits a significant thermoelectric effect at ambient temperature. Specifically, the Seebeck coefficient of the Ni-HITP film is 11.9 $\mu V\ K^{-1}$, a value that indicates its ability to effectively generate potential difference under temperature difference conditions. In addition, the microstructure of the Ni-HITP film presents a porous network, and this unique structure endows it with a strong phonon scattering ability, which significantly reduces the thermal conductivity, which is about 0.21 $W\ m^{-1}\ K^{-1}$. This low thermal conductivity property is favorable for improving the thermoelectric conversion efficiency. At the same time, the Ni-HITP film also has a high electrical conductivity, which enables its thermoelectric conversion efficiency (*ZT* value) to reach 1.19×10^{-3} at room temperature (Fig. 23g–i). This *ZT* value, although not extremely high among current thermoelectric materials, has shown good potential for thermoelectric properties for a novel material such as Ni-HITP, providing an important basis and direction for further optimization of its thermoelectric properties in the future.

4.4.5. Catalyst. C-MOFs have achieved substantial advancements in catalysis attributed to their elevated specific surface area, tunable porosity, an abundance of metal centres, and high electrical conductivity, furnishing a substantial quantity of active sites for the reaction and allowing optimised design for specific electrocatalytic reactions.[133] In 2016, the Sun team successfully constructed monolithic, electrochemically excellent MOF (metal–organic framework) thin films on conductive FTO (fluorine-doped tin dioxide) electrodes by liquid-phase epitaxy.[134] This MOF film prepared by the epitaxial growth method exhibited an extremely high Faraday efficiency of 93.5% when applied to the electrocatalytic reaction of CO_2 reduction to CO (Fig. 24a–c). This efficiency demonstrates that this MOF film is capable of efficiently converting electrical energy into chemical energy during the electrocatalytic process, converting CO_2 into valuable CO products. In addition, this high-quality monolithic coating offers a significant current density advantage of more than 2 $mA\ cm^{-2}$, a value that is at least ten times higher than previously reported MOF films (Fig. 24d). This superior current density not only improves the rate of the electrocatalytic reaction, but also offers the possibility of achieving large-scale, highly efficient electrocatalytic conversion of CO_2, which provides a potential solution to combat the global carbon emission problem.

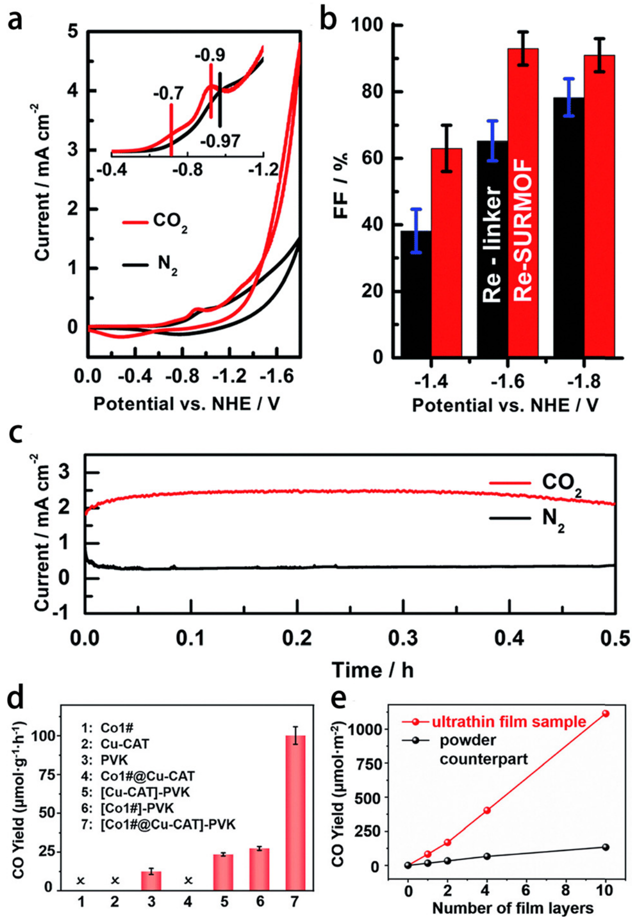

Fig. 24 (a) Cyclic voltammogram of the Re-MOF within a saturated electrolyte under a scan rate of 100 mV s^{-1}. (b) Faradaic efficiency of the CO_2 reduction catalyzed by the Re-MOF and the Re-linker (0.5 mM) as a function of the applied potential. The electrolyte was saturated with either CO_2 or N_2. (c) Current density of the CO_2 reduction catalyzed by the Re-MOF in electrolytes saturated with CO_2 and N_2 at a potential of 1.6 V *versus* the NHE during the initial half-hour. (d) Photocatalytic CO_2RR performance of [Co1#@Cu-HHTP]–PVK and control experiments. (e) Photocatalytic CO_2RR performance after 4 h for the multilayer film catalyst device and powder counterpart. (Adapted from ref. 131 and 70 with permission from Royal Society of Chemistry, and American Chemical Society, Copyright 2016 and 2024, respectively.)

Recently, Hu's team employed an innovative electrostatic-driven strategy to successfully immobilise dinuclear metal molecular catalysts (DMCs) and perovskite quantum dot photosensitisers (PVKs) in the channels and on the surface of C-MOF (covalent metal–organic frameworks) ultrathin films by a steric-blocking synergistic effect, resulting in the preparation of a novel [DMC@cMOF]–PVK thin-film photocatalyst.[76] The design of this photocatalyst makes full use of the efficient catalytic activity of DMC and the photosensitive properties of PVK, while the high photocatalytic performance is achieved with the high specific surface area and good pore structure of C-MOF ultrathin films. In the experiment of photocatalytic reduction of CO_2 with H_2O as the electron donor, the [DMC@cMOF]–PVK photocatalysts showed excellent performance with a CO yield of 133.36 $\mu mol\ g^{-1}\ h^{-1}$, which is a value far exceeding the performance of PVK alone as well as the DMC–PVK composites (as shown in Fig. 24e). To further enhance the photocatalytic performance, Hu's team cleverly integrated the [DMC@cMOF]–PVK multilayer membrane structure with excellent light transmittance into the film. This multilayer membrane design not only increases the number of active sites of the photocatalyst, but also optimises the light absorption and scattering pathways, thus significantly increasing the CO yield per unit area. The experimental results showed that the 10-layer device achieved a CO yield of 1115.92 $\mu mol^{-1}\ m^{-2}$ in 4 h, a value that was eight times higher than that of the conventional powder device. This achievement not only demonstrates the great potential of [DMC@cMOF]–PVK thin-film photocatalysts in the field of CO_2

photocatalytic reduction, but also provides new ideas and methods for the development of high-performance photocatalytic materials.

5. Summary and outlook

In the past few years, C-MOFs, representing a new category of semiconductor materials, have garnered significant interest within the scientific community. C-MOF films are distinguished by their structural diversity, porosity, and excellent electrical conductivity, positioning them as a focal point in MOF research. This paper reviews the primary methods, growth mechanisms, and applications of C-MOF thin films synthesized using interface-assisted techniques.

Despite notable advancements in the study of C-MOF films in recent years, this field remains nascent and is confronted with various challenges and obstacles.

(1) In terms of the universality of thin films prepared by interface-assisted methods: At present, interface-assisted methods (*e.g.*, gas–liquid interface, liquid–liquid interface) have been successfully used to synthesise some C-MOF thin films (*e.g.*, Ni-HITP, Cu-BHT, *etc.*) but their universality has not yet been sufficiently verified. Existing methods mostly rely on planar conjugated ligands (*e.g.*, HITP, BHT), while MOFs with complex topologies (*e.g.*, 3D conjugated or flexible ligands) are difficult to prepare using interfacial methods. Multifunctional ligands with both solubility and interfacial self-assembly capabilities can be developed.

(2) In terms of growth mechanism: although this method has been used to fabricate C-MOF films, the underlying growth mechanism needs to be further investigated. The interfacial growth process can be observed in real time by using synchrotron X-ray scattering (GISAXS) or *in situ* AFM. Molecular dynamics (MD) can also be used to simulate the ligand–metal interaction energy at the interface and predict optimal growth conditions.

(3) Scale-up of large-area, high-quality films: laboratory-prepared films are typically 1–10 cm^2 in size, whereas industrial applications require square metres of continuous film, so there have been challenges in scaling up the manufacture of C-MOF films for industrial use. Therefore, further studies are required.

(4) Future application scenarios and interdisciplinary integration: the flexibility and biocompatibility of C-MOF films can be utilized to develop high-resolution microelectrode arrays. It can also be combined with semiconductor processes to develop graphical etching technology for MOF-based integrated circuits.

Despite these challenges, the structural designability and functional programmability of conductive MOF films hold promise as core components of future electronic materials. Continued investment in basic research and application development will accelerate the realization of this vision.

Data availability

No primary research results, software or code have been included and no new data were generated or analysed as part of this review.

Conflicts of interest

There are no conflicts to declare.

Acknowledgements

We gratefully acknowledge financial support from the National Natural Science Foundation of China (22325109, 22171263, and 62227815), the Fujian Science & Technology Innovation Laboratory for Optoelectronic Information of China (2021ZR101), the Self-deployment Project Research Program of Haixi Institutes, Chinese Academy of Sciences (CXZX-2022-GH09 and CXZX-2023-GS03), the Natural Science Foundation of Shanxi Province (202303021222189), and the Scientific Foundation of the State Key Laboratory of Structural Chemistry (20240036).

References

1 B. Achenbach, A. Yurdusen, N. Stock, G. Maurin and C. Serre, *Adv. Mater.*, 2025, 2411359.
2 N. F. Suremann, B. D. McCarthy, W. Gschwind, A. Kumar, B. A. Johnson, L. Hammarström and S. Ott, *Chem. Rev.*, 2023, **123**, 6545–6611.
3 B. P. Carpenter, A. R. Talosig, B. Rose, G. Di Palma and J. P. Patterson, *Chem. Soc. Rev.*, 2023, **52**, 6918–6937.
4 M. Xu, W. Q. Tang, S. S. Meng and Z. Y. Gu, *Chem. Soc. Rev.*, 2025, **54**, 1613–1633.
5 X. Y. Qiu and R. Wang, *Coord. Chem. Rev.*, 2025, **526**, 216356.
6 H. Y. Li, X. J. Kong, S. D. Han, J. D. Pang, T. He, G. M. Wang and X. H. Bu, *Chem. Soc. Rev.*, 2024, **53**, 5626–5676.
7 X. Y. Luo, M. Zhang, Y. B. Hu, Y. Xu, H. F. Zhou, Z. J. Xu, Y. X. Hao, S. Chen, S. F. Chen, Y. W. Luo, Y. L. Lin and J. J. Zhao, *Science*, 2024, **385**, 647–651.
8 N. Y. Huang, Y. T. Zheng, D. Chen, Z. Y. Chen, C. Z. Huang and Q. Xu, *Chem. Soc. Rev.*, 2023, **52**, 7949–8004.
9 N. Hanikel, X. Pei, J. Sauer, L. Gagliardi and O. M. Yaghi, *Science*, 2021, **374**, 454–459.
10 B. An, Z. Li, Y. Song, J. Z. Zhang, L. Z. Zeng, C. Wang and W. B. Lin, *Nat. Catal.*, 2019, **2**, 709–717.
11 H. Furukawa, K. E. Cordova, M. O'Keeffe and O. M. Yaghi, *Science*, 2013, **341**, 1230444.
12 H.-C. Zhou, J. R. Long and O. M. Yaghi, *Chem. Rev.*, 2012, **112**, 673–674.
13 L. Q. Ma, C. Abney and W. B. Lin, *Chem. Soc. Rev.*, 2009, **38**, 1248–1256.
14 Z. S. Yuan, H. N. Chai, Y. Huang, Z. Y. Zhang, W. Q. Tan, Y. J. Sun, J. P. Ma and G. Y. Zhang, *Coord. Chem. Rev.*, 2025, **527**, 216385.
15 P. H. Tong, J. J. Yang, Y. F. Zhou, Y. F. Tang, M. T. Tang, Y. Zang, Y. F. Pan, L. W. Dong, Y. X. Tan, K. T. Nam, X. L. Hu, H. Huang, J. Li, H. Y. Wang, T. D. James, J. Yoon and X. P. He, *Coord. Chem. Rev.*, 2025, **526**, 21638.
16 L. L. Chai, R. Li, Y. Z. Sun, K. Zhou and J. Q. Pan, *Adv. Mater.*, 2025, **37**, 2413658.
17 X. L. Yan, X. Su, J. Chen, C. Jin and L. Chen, *Angew. Chem., Int. Ed.*, 2023, **62**, e202305408.
18 Y. Cheng, S. J. Datta, S. Zhou, J. Jia, O. Shekhah and M. Eddaoudi, *Chem. Soc. Rev.*, 2022, **51**, 8300–8350.
19 M. C. Wang, R. H. Dong and X. L. Feng, *Chem. Soc. Rev.*, 2021, **50**, 2764–2793.
20 L. S. Xie, G. Skorupskii and M. Dinca, *Chem. Rev.*, 2020, **120**, 8536–8580.
21 X. Gao, Y. Dong, S. W. Li, J. W. Zhou, L. Wang and B. Wang, *Electrochem. Energy Rev.*, 2020, **3**, 81–126.
22 I. Stassen, N. C. Burtch, A. A. Talin, P. Falcaro, M. D. Allendorf and R. Ameloot, *Chem. Soc. Rev.*, 2017, **46**, 3185–3241.
23 T. Kitao, Y. Y. Zhang, S. Kitagawa, B. Wang and T. Uemura, *Chem. Soc. Rev.*, 2017, **46**, 3108–3133.
24 H. C. Zhou, J. R. Long and O. M. Yaghi, *Chem. Rev.*, 2012, **112**, 673–674.

25 P. B. Geng, L. Wang, M. Du, Y. Bai, W. T. Li, Y. F. Liu, S. Q. Chen, P. Braunstein, Q. Xu and H. Pang, *Adv. Mater.*, 2022, **34**, 2107836.

26 A. A. Talin, A. Centrone, A. C. Ford, M. E. Foster, V. Stavila, P. Haney, R. A. Kinney, V. Szalai, F. El Gabaly, H. P. Yoon, F. Léonard and M. D. Allendorf, *Science*, 2014, **343**, 66–69.

27 H. L. Jiang, B. Liu, Y. Q. Lan, K. Kuratani, T. Akita, H. Shioyama, F. Q. Zong and Q. Xu, *J. Am. Chem. Soc.*, 2011, **133**, 11854–11857.

28 Z. Li, J. Liu, L. Feng, Y. Pan, J. Tang, H. Li, G. Cheng, Z. Li, J. Shi and Y. Xu, *Nano Lett.*, 2023, **23**, 637–644.

29 P. Z. Moghadam, Y. G. Chung and R. Q. Snurr, *Nat. Energy*, 2024, **9**, 121–133.

30 Y. Zhao, L. Wu, K. Wu, R.-J. Wei, H. Zeng, H. Pang, W. Lu and D. Li, *Coord. Chem. Rev.*, 2025, **524**, 216302.

31 R. Saha and C. J. G. García, *Chem. Soc. Rev.*, 2024, 9490–9559.

32 B. Check, K. Bairley, J. Santarelli, H. T. B. Pham and J. Park, *ACS Mater. Lett.*, 2025, 465–488.

33 X. Y. Wang, R. A. Borse, G. Wang, Z. Xiao, H. Zhu, Y. L. Sun, Z. F. Qian, S. K. Zhong and R. H. Wang, *Mater. Today Energy*, 2024, **44**, 101652.

34 M. Y. Yang, Y. Zhang, R. L. Zhu, J. J. Tan, J. X. Liu, W. Zhang, M. Zhou and Z. Meng, *Angew. Chem., Int. Ed.*, 2024, **63**, e202405333.

35 J. D. Wang, T. Y. Chen, M. Jeon, J. J. Oppenheim, B. W. Tan, J. Kim and M. Dinca, *J. Am. Chem. Soc.*, 2024, **146**, 20500–20507.

36 Q. Zhang, S. Jiang, T. T. Lv, Y. Peng and H. Pang, *Adv. Mater.*, 2023, **35**, 2305532.

37 L. L. Kang, M. Xue, Y. Y. Liu, Y. H. Yu, Y. R. Liu and G. Li, *Coord. Chem. Rev.*, 2022, **452**, 214301.

38 W. H. Li, W. H. Deng, G. E. Wang and G. Xu, *Energychem*, 2020, **2**, 100029.

39 B. L. Cui, X. Y. Lang, Z. X. Ren, L. N. Cheng, D. C. Yang and W. Wang, *Sens. Actuators, B*, 2025, **423**, 136817.

40 H. T. B. Pham, J. Y. Choi, M. Stodolka and J. Park, *Acc. Chem. Res.*, 2024, **57**, 580–589.

41 H. Roh, D. H. Kim, Y. S. Cho, Y. M. Jo, J. A. del Alamo, H. J. Kulik, M. Dinca and A. Gumyusenge, *Adv. Mater.*, 2024, **36**, 2312382.

42 R. H. Dong, Z. T. Zhang, D. C. Tranca, S. Q. Zhou, M. C. Wang, P. Adler, Z. Q. Liao, F. Liu, Y. Sun, W. J. Shi, Z. Zhang, E. Zschech, S. C. B. Mannsfeld, C. Felser and X. L. Feng, *Nat. Commun.*, 2018, **9**, 2637.

43 J. Park, M. Lee, D. W. Feng, Z. H. Huang, A. C. Hinckley, A. Yakoyenko, X. D. Zou, Y. Cui and Z. A. Bao, *J. Am. Chem. Soc.*, 2018, **140**, 10315–10323.

44 W. B. Li, L. Sun, J. S. Qi, P. Jarillo-Herrero, M. Dinca and J. Li, *Chem. Sci.*, 2017, **8**, 2859–2867.

45 M. G. Campbell, D. Sheberla, S. F. Liu, T. M. Swager and M. Dinca, *Angew. Chem., Int. Ed.*, 2015, **54**, 4349–4352.

46 L. S. Xie, G. Skorupskii and M. Dinca, *Chem. Rev.*, 2020, **120**, 8536–8580.

47 X. Fang, J. Y. Choi, M. Stodolka, H. T. Pham and J. Park, *Acc. Chem. Res.*, 2024, **57**, 2316–2325.

48 L. Liu, Q. Xu and Q. L. Zhu, *Adv. Energy Sustainability Res.*, 2021, **2**, 2100100.

49 S. Tao, J. Wang and J. Zhang, *ACS Nano*, 2025, **19**, 9484–9512.

50 L. Niu, T. Z. Wu, M. Chen, L. Yang, J. J. Yang, Z. X. Wang, A. A. Kornyshev, H. L. Jiang, S. Bi and G. Feng, *Adv. Mater.*, 2022, **34**, 2200999.

51 X. H. Ren, G. C. Liao, Z. J. Li, H. Qiao, Y. Zhang, X. Yu, B. Wang, H. Tan, L. Shi, X. Qi and H. Zhang, *Coord. Chem. Rev.*, 2021, **435**, 213781.

52 J. Liu and C. Wöll, *Chem. Soc. Rev.*, 2017, **46**, 5730–5770.

53 S. J. Xie, Z. Y. Zhou, X. Zhang and J. Fransaer, *Chem. Soc. Rev.*, 2023, **52**, 4292–4312.

54 L. A. Cao and M. Wei, *Acta Chim. Sin.*, 2022, **80**, 1042–1056.

55 Z. Y. Wang, G. Wang, H. Y. Qi, M. Wang, M. C. Wang, S. Park, H. P. Wang, M. H. Yu, U. Kaiser, A. Fery, S. Q. Zhou, R. H. Dong and X. L. Feng, *Chem. Sci.*, 2020, **11**, 7665–7671.

56 L. H. Wang, H. Sahabudeen, T. Zhang and R. H. Dong, *npj 2D Mater. Appl.*, 2018, **2**, 26.

57 X. M. Zhang, H. Y. Nan, S. Q. Xiao, X. Wan, X. F. Gu, A. J. Du, Z. H. Ni and K. Ostrikov, *Nat. Commun.*, 2019, **10**, 598.

58 Y. X. Chen, K. L. Liu, J. X. Liu, T. R. Lv, B. Wei, T. Zhang, M. Q. Zeng, Z. C. Wang and L. Fu, *J. Am. Chem. Soc.*, 2018, **140**, 16392–16395.

59 I. Stassen, M. Styles, G. Grenci, H. Van Gorp, W. Vanderlinden, S. De Feyter, P. Falcaro, D. De Vos, P. Vereecken and R. Ameloot, *Nat. Mater.*, 2016, **15**, 304–310.

60 E. Redel, Z. B. Wang, S. Walheim, J. X. Liu, H. Gliemann and C. Wöll, *Appl. Phys. Lett.*, 2013, **103**, 091903.

61 H. P. Wang, Q. R. Wu, H. B. Fu, L. Z. Wu and X. L. Feng, *Chem. Commun.*, 2022, **58**, 12384–12398.

62 T. Kambe, R. Sakamoto, K. Hoshiko, K. Takada, M. Miyachi, J. H. Ryu, S. Sasaki, J. Kim, K. Nakazato, M. Takata and H. Nishihara, *J. Am. Chem. Soc.*, 2013, **135**, 2462–2465.

63 T. Pal, T. Kambe, T. Kusamoto, M. L. Foo, R. Matsuoka, R. Sakamoto and H. Nishihara, *ChemPlusChem*, 2015, **80**, 1255–1258.

64 X. Huang, P. Sheng, Z. Y. Tu, F. J. Zhang, J. H. Wang, H. Geng, Y. Zou, C. A. Di, Y. P. Yi, Y. M. Sun, W. Xu and D. B. Zhu, *Nat. Commun.*, 2015, **6**, 7408.

65 N. Lahiri, N. Lotfizadeh, R. Tsuchikawa, V. V. Deshpande and J. Louie, *J. Am. Chem. Soc.*, 2017, **139**, 19–22.

66 X. J. Bai, D. Chen, L. L. Li, L. Shao, W. X. He, H. Chen, Y. N. Li, X. M. Zhang, L. Y. Zhang, T. Q. Wang, Y. Fu and W. Qi, *ACS Appl. Mater. Interfaces*, 2018, **10**, 25960–25966.

67 I. F. Chen, C. F. Lu and W. F. Su, *Langmuir*, 2018, **34**, 15754–15762.

68 R. Dong, P. Han, H. Arora, M. Ballabio, M. Karakus, Z. Zhang, C. Shekhar, P. Adler, P. Petkov, A. Erbe, S. C. B. Mannsfeld, C. Felser, T. Heine, M. Bonn, X. L. Feng and E. Canovas, *Nat. Mater.*, 2018, **17**, 1027–1032.

69 K. Ohta, Y. Hiramatsu, K. Takahashi, M. Suzuki, H. Yamada and K. Tominaga, *J. Photochem. Photobiol., A*, 2020, **400**, 112693.

70 V. Rubio-Giménez, M. Galbiati, J. Castells-Gil, N. Almora-Barrios, J. Navarro-Sánchez, G. Escorcia-Ariza, M. Mattera, T. Arnold, J. Rawle, S. Tatay, E. Coronado and C. Martí-Gastaldo, *Adv. Mater.*, 2018, **30**, 1704291.

71 G. D. Wu, J. H. Huang, Y. Zang, J. He and G. Xu, *J. Am. Chem. Soc.*, 2017, **139**, 1360–1363.

72 R. H. Dong, M. Pfeffermann, H. W. Liang, Z. K. Zheng, X. Zhu, J. Zhang and X. L. Feng, *Angew. Chem., Int. Ed.*, 2015, **54**, 12058–12063.

73 T. Ohata, A. Nomoto, T. Watanabe, I. Hirosawa, T. Makita, J. Takeya and R. Makiura, *ACS Appl. Mater. Interfaces*, 2021, **13**, 54570–54578.

74 Z. Y. Wang, L. S. Walter, M. Wang, P. S. Petkov, B. K. Liang, H. Y. Qi, N. N. Nguyen, M. Hambsch, H. X. Zhong, M. C. Wang, S. Park, L. Renn, K. Watanabe, T. Taniguchi, S. C. B. Mannsfeld, T. Heine, U. Kaiser, S. Q. Zhou, R. T. Weitz, X. L. Feng and R. H. Dong, *J. Am. Chem. Soc.*, 2021, **143**, 13624–13632.

75 J. X. Liu, Y. X. Chen, X. Huang, Y. H. Ren, M. Hambsch, D. Bodesheim, D. Pohl, X. D. Li, M. Deconinck, B. W. Zhang, M. Löffler, Z. Q. Liao, F. X. Zhao, A. Dianat, G. Cuniberti, Y. Vaynzof, J. F. Gao, J. C. Hao, S. C. B. Mannsfeld, X. L. Feng and R. H. Dong, *Nat. Synth.*, 2024, **3**, 715–726.

76 K. Yuan, K. Y. Tao, T. Q. Song, Y. Zhang, T. Zhang, F. Wang, S. M. Duan, Z. Chen, L. J. Li, X. T. Zhang, D. C. Zhong, Z. Y. Tang, T. B. Lu and W. P. Hu, *J. Am. Chem. Soc.*, 2024, **146**, 6893–6904.

77 S. Zhou, O. Shekhah, A. Ramírez, P. B. Lyu, E. Abou-Hamad, J. T. Jia, J. T. Li, P. M. Bhatt, Z. Y. Huang, H. Jiang, T. Jin, G. Maurin, J. Gascon and M. Eddaoudi, *Nature*, 2022, **606**, 706–712.

78 Y. Chen, X. L. Gong and J. G. Gai, *Adv. Sci.*, 2016, **3**, 1500343.

79 O. Shekhah, J. Liu, R. A. Fischer and C. Wöll, *Chem. Soc. Rev.*, 2011, **40**, 1081–1106.

80 J. X. Liu and C. Wöll, *Chem. Soc. Rev.*, 2017, **46**, 5730–5770.

81 J. L. Zhuang, A. Terfort and C. Wöll, *Coord. Chem. Rev.*, 2016, **307**, 391–424.

82 O. Shekhah, K. Hirai, H. Wang, H. Uehara, M. Kondo, S. Diring, D. Zacher, R. A. Fischer, O. Sakata, S. Kitagawa, S. Furukawa and C. Wöll, *Dalton Trans.*, 2011, **40**, 4954–4958.

83 M. S. Yao, X. J. Lv, Z. H. Fu, W. H. Li, W. H. Deng, G. D. Wu and G. Xu, *Angew. Chem., Int. Ed.*, 2017, **56**, 16510–16514.

84 X. Y. Song, X. Y. Wang, Y. S. Li, C. Z. Zheng, B. W. Zhang, C. A. Di, F. Li, C. Jin, W. B. Mi, L. Chen and W. P. Hu, *Angew. Chem., Int. Ed.*, 2020, **59**, 1118–1123.

85 Y. X. Liu, Y. N. Wei, M. H. Liu, Y. C. Bai, X. Y. Wang, S. C. Shang, C. S. Du, W. Q. Gao, J. Y. Chen and Y. Q. Liu, *Adv. Mater.*, 2021, **33**, 2007741.

86 Z. Z. Ma, Q. H. Li, Z. R. Wang, Z. G. Gu and J. Zhang, *Nat. Commun.*, 2022, **13**, 720.

87 D. G. Ha, M. Rezaee, Y. M. Han, S. A. Siddiqui, R. W. Day, L. S. Xie, B. J. Modtland, D. A. Muller, J. Kong, P. Kim, M. Dinca and M. A. Baldo, *ACS Cent. Sci.*, 2021, **7**, 104–109.

88 K. Yuan, T. Q. Song, X. T. Zhu, B. L. Li, B. Han, L. Zheng, J. F. Li, X. T. Zhang and W. P. Hu, *Small*, 2019, **15**, 1804845.

89 Q. Li, J. Gies, X. J. Yu, Y. Gu, A. Terfort and M. Kind, *Chem. – Eur. J.*, 2020, **26**, 5185–5189.

90 O. Shekhah, *Materials*, 2010, **3**, 1302–1315.

91 G. Delen, Z. Ristanovic, L. D. B. Mandemaker and B. M. Weckhuysen, *Chem. – Eur. J.*, 2018, **24**, 187–195.

92 J. Lau, A. E. Trojniak, M. J. Maraugha, A. J. VanZanten, A. J. Osterbaan, A. C. Serino, M. L. Ohnsorg, K. M. Cheung, D. S. Ashby, P. S. Weiss, B. S. Dunn and M. E. Anderson, *Chem. Mater.*, 2019, **31**, 8977–8986.

93 J. P. Nan, X. L. Dong, W. J. Wang, W. Q. Jin and N. P. Xu, *Langmuir*, 2011, **27**, 4309–4312.

94 O. Shekhah, H. Wang, S. Kowarik, F. Schreiber, M. Paulus, M. Tolan, C. Sternemann, F. Evers, D. Zacher, R. A. Fischer and C. Wöll, *J. Am. Chem. Soc.*, 2007, **129**, 15118–15119.

95 C. Munuera, O. Shekhah, H. Wang, C. Wöll and C. Ocal, *Phys. Chem. Chem. Phys.*, 2008, **10**, 7257–7261.

96 O. Shekhah, H. Wang, D. Zacher, R. A. Fischer and C. Wöll, *Angew. Chem., Int. Ed.*, 2009, **48**, 5038–5041.

97 V. Stavila, J. Volponi, A. M. Katzenmeyer, M. C. Dixon and M. D. Allendorf, *Chem. Sci.*, 2012, **3**, 1531–1540.

98 J. L. Zhuang, M. Kind, C. M. Grytz, F. Farr, M. Diefenbach, S. Tussupbayev, M. C. Holthausen and A. Terfort, *J. Am. Chem. Soc.*, 2015, **137**, 8237–8243.

99 R. Zheng, Z. H. Fu, W. H. Deng, Y. Y. Wen, A. Q. Wu, X. L. Ye and G. Xu, *Angew. Chem., Int. Ed.*, 2022, **61**, e202212797.

100 C. L. Wang, H. L. Dong, L. Jiang and W. P. Hu, *Chem. Soc. Rev.*, 2018, **47**, 422–500.

101 S. J. Wang, X. Chen, C. Zhao, Y. X. Kong, B. J. Lin, Y. Y. Wu, Z. Z. Bi, Z. Y. Xuan, T. Li, Y. X. Li, W. Zhang, E. Ma, Z. R. Wang and W. Ma, *Nat. Electron.*, 2023, **6**, 281–291.

102 B. F. Wang, Y. Y. Luo, B. Liu and G. T. Duan, *ACS Appl. Mater. Interfaces*, 2019, **11**, 35935–35940.

103 W. T. Koo, J. S. Jang and I. D. Kim, *Chem*, 2019, **5**, 1938–1963.

104 M. G. Campbell, S. F. Liu, T. M. Swager and M. Dinca, *J. Am. Chem. Soc.*, 2015, **137**, 13780–13783.

105 H. Y. Yuan, N. X. Li, W. D. Fan, H. Cai and D. Zhao, *Adv. Sci.*, 2022, **9**, 2104374.

106 A. Q. Wu, W. Q. Wang, H. B. Zhan, L. A. Cao, X. L. Ye, J. J. Zheng, P. N. Kumar, K. Chiranjeevulu, W. H. Deng, G. E. Wang, M. S. Yao and G. Xu, *Nano Res.*, 2021, **14**, 438–443.

107 Y. Lin, W. H. Li, Y. Y. Wen, G. E. Wang, X. L. Ye and G. Xu, *Angew. Chem., Int. Ed.*, 2021, **60**, 25758–25761.

108 V. Stavila, A. A. Talin and M. D. Allendorf, *Chem. Soc. Rev.*, 2014, **43**, 5994–6010.

109 H. Arora, R. H. Dong, T. Venanzi, J. Zscharschuch, H. Schneider, M. Helm, X. L. Feng, E. Cánovas and A. Erbe, *Adv. Mater.*, 2020, **32**, 1907063.

110 S. H. Liu, Y. C. Wang, C. M. Chang, T. Yasuda, N. Fukui, H. Maeda, P. Long, K. Nakazato, W. B. Jian, W. F. Xie, K. Tsukagoshi and H. Nishihara, *Nanoscale*, 2020, **12**, 6983–6990.

111 Z. W. Jin, J. Yan, X. Huang, W. Xu, S. Y. Yang, D. B. Zhu and J. Z. Wang, *Nano Energy*, 2017, **40**, 376–381.

112 Z. T. Li, W. Zeng and Y. Q. Li, *Molecules*, 2023, **28**, 2303775.

113 X. X. Jiang, C. J. Zhao, C. J. Zhong and J. P. Li, *Prog. Chem.*, 2017, **29**, 1206–1214.

114 M. Daniel, G. Mathew, M. Anpo and B. Neppolian, *Coord. Chem. Rev.*, 2022, **468**, 214627.

115 C. H. Chuang and C. W. Kung, *Electroanalysis*, 2020, **32**, 1885–1895.

116 Q. Zhao, S. H. Li, R. L. Chai, X. Ren and C. Zhang, *ACS Appl. Mater. Interfaces*, 2020, **12**, 7504–7509.

117 X. Chen, J. J. Dong, K. Chi, L. J. Wang, F. Xiao, S. Wang, Y. Zhao and Y. Q. Liu, *Adv. Funct. Mater.*, 2021, **31**, 2102855.

118 R. M. Stolz, A. F. Kolln, B. C. Rocha, A. Brinks, A. M. Eagleton, L. Mendecki, H. Vashisth and K. A. Mirica, *ACS Nano*, 2022, 13869–13883.

119 M. Jayalakshmi and K. Balasubramanian, *Int. J. Electrochem. Sci.*, 2008, **3**, 1196–1217.

120 J. L. Sun, B. C. Luo and H. X. Li, *Adv. Energy Sustainability Res.*, 2022, **3**, 2100191.

121 Y. L. Wang, Z. F. Liu, J. J. Li, C. Y. Ge, X. Ye, Y. X. Xie, P. C. Zhao and J. J. Fei, *Nano Energy*, 2025, **135**, 110655.

122 L. Z. Guo, J. F. Sun, J. X. Wei, Y. Liu, L. R. Hou and C. Z. Yuan, *Carbon Energy*, 2020, **2**, 203–222.

123 K. F. Xiao, D. L. Jiang, R. Amal and D. W. Wang, *Adv. Mater.*, 2018, **30**, 18000400.

124 D. Sheberla, J. C. Bachman, J. S. Elias, C. J. Sun, Y. Shao-Horn and M. Dinca, *Nat. Mater.*, 2017, **16**, 220–224.

125 W. W. Zhao, T. T. Chen, W. K. Wang, S. H. Bi, M. Y. Jiang, K. Y. Zhang, S. J. Liu, W. Huang and Q. Zhao, *Adv. Mater. Interfaces*, 2021, **8**, 2100308.

126 S. Behboudikhiavi, G. Chanteux, B. Babu, S. Faniel, F. Marlec, K. Robert, D. Magnin, F. Lucaccioni, J. O. Omale, P. Apostol, L. Piraux, C. Lethien and A. Vlad, *Small*, 2024, **20**, 2401509.

127 W. Han, R. K. Kawakami, M. Gmitra and J. Fabian, *Nat. Nanotechnol.*, 2014, **9**, 794–807.

128 G. S. Yang, L. A. Sang, C. Zhang, N. Ye, A. Hamilton, M. S. Fuhrer and X. L. Wang, *Nat. Rev. Phys.*, 2023, **5**, 466–482.

129 M. Haras and T. Skotnicki, *Nano Energy*, 2018, **54**, 461–476.

130 M. Martín-González, O. Caballero-Calero and P. Díaz-Chao, *Renewable Sustainable Energy Rev.*, 2013, **24**, 288–305.

131 L. Sun, B. L. Liao, D. Sheberla, D. Kraemer, J. W. Zhou, E. A. Stach, D. Zakharov, V. Stavila, A. A. Talin, Y. C. Ge, M. D. Allendorf, G. Chen, F. Léonard and M. Dinca, *Joule*, 2017, **1**, 168–177.

132 Z. J. Chen, Y. T. Cui, Y. G. Jin, L. Y. Liu, J. Yan, Y. Sun, Y. Zou, Y. M. Sun, W. Xu and D. B. Zhu, *J. Mater. Chem. C*, 2020, **8**, 8199–8205.

133 C. P. Wan, J. D. Yi, R. Cao and Y. B. Huang, *Chin. J. Struct. Chem.*, 2022, **41**, 2205001–2205014.

134 L. Ye, J. X. Liu, Y. Gao, C. H. Gong, M. Addicoat, T. Heine, C. Wöll and L. C. Sun, *J. Mater. Chem. A*, 2016, **4**, 15320–15326.